Cell Reports

Article

Reduced GABAergic Neuron Excitability, Altered Synaptic Connectivity, and Seizures in a KCNT1 Gain-of-Function Mouse Model of Childhood Epilepsy

Graphical Abstract

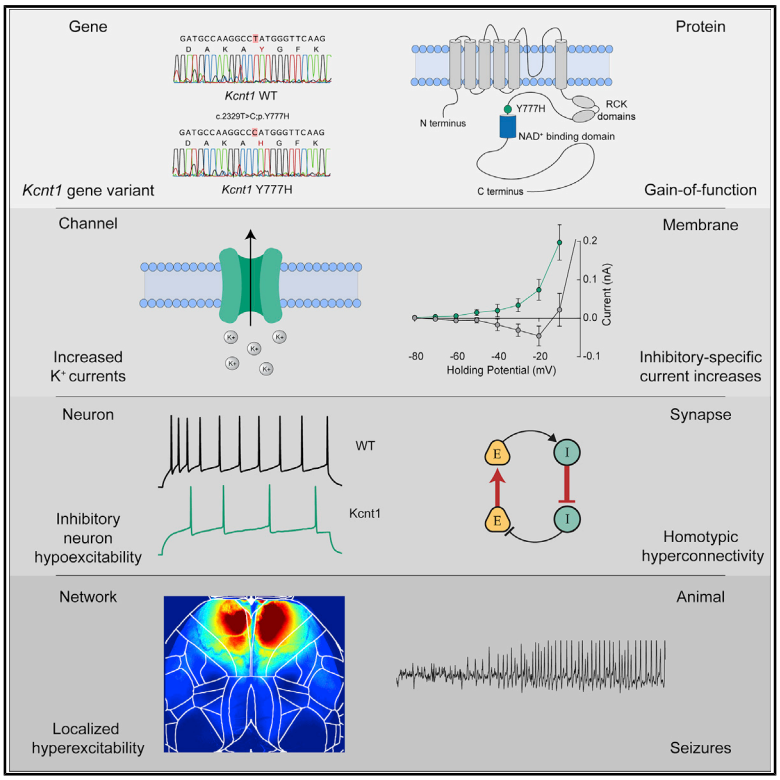

Highlights

- In humans, *KCNT1* GOF variants cause severe epilepsy and intellectual disability
- KCNT1 GOF increases subthreshold K_{Na} currents selectively in GABAergic neurons
- KCNT1 GOF impairs GABAergic neuron excitability and alters synaptic connectivity
- Mice expressing a *Kcnt1* GOF variant exhibit seizures and cognitive impairments

Authors

Amy N. Shore, Sophie Colombo, William F. Tobin, ..., Michael J. Boland, Wayne N. Frankel, Matthew C. Weston

Correspondence

mcweston@uvm.edu

In Brief

Shore et al. generate a mouse model of a GOF variant in the Na^+-activated K^+ channel gene *KCNT1* that causes a childhood epilepsy disorder. In mice, KCNT1 GOF reduces the excitability of cortical GABAergic neurons and increases homotypic synaptic connectivity, resulting in disrupted E/I balance, network hyperexcitability, and seizures.

Shore et al., 2020, Cell Reports *33*, 108303
October 27, 2020
https://doi.org/10.1016/j.celrep.2020.108303

CellPress

Cell Reports

CellPress
OPEN ACCESS

Article

Reduced GABAergic Neuron Excitability, Altered Synaptic Connectivity, and Seizures in a KCNT1 Gain-of-Function Mouse Model of Childhood Epilepsy

Amy N. Shore,[1,9] Sophie Colombo,[2,9] William F. Tobin,[1] Sabrina Petri,[2] Erin R. Cullen,[1] Soledad Dominguez,[2] Christopher D. Bostick,[2] Michael A. Beaumont,[2,3] Damian Williams,[2] Dion Khodagholy,[4] Mu Yang,[2] Cathleen M. Lutz,[5] Yueqing Peng,[2,6] Jennifer N. Gelinas,[2,7] David B. Goldstein,[2,8] Michael J. Boland,[2,8] Wayne N. Frankel,[2,7] and Matthew C. Weston[1,10,*]

[1]Department of Neurological Sciences, University of Vermont, Burlington, VT 05405, USA
[2]Institute for Genomic Medicine, Columbia University, New York, NY 10032, USA
[3]Axion BioSystems, Atlanta, GA 30309, USA
[4]Department of Electrical Engineering, Columbia University, New York, NY 10032, USA
[5]The Jackson Laboratory, Bar Harbor, ME 04609, USA
[6]Department of Pathology and Cell Biology, Columbia University, New York, NY 10032, USA
[7]Department of Neurology, Columbia University, New York, NY 10032, USA
[8]Department of Genetics and Development, Columbia University, New York, NY 10032, USA
[9]These authors contributed equally
[10]Lead Contact
*Correspondence: mcweston@uvm.edu
https://doi.org/10.1016/j.celrep.2020.108303

SUMMARY

Gain-of-function (GOF) variants in K^+ channels cause severe childhood epilepsies, but there are no mechanisms to explain how increased K^+ currents lead to network hyperexcitability. Here, we introduce a human Na^+-activated K^+ (K_{Na}) channel variant (*KCNT1*-Y796H) into mice and, using a multiplatform approach, find motor cortex hyperexcitability and early-onset seizures, phenotypes strikingly similar to those of human patients. Although the variant increases K_{Na} currents in cortical excitatory and inhibitory neurons, there is an increase in the K_{Na} current across subthreshold voltages only in inhibitory neurons, particularly in those with non-fast-spiking properties, resulting in inhibitory-neuron-specific impairments in excitability and action potential (AP) generation. We further observe evidence of synaptic rewiring, including increases in homotypic synaptic connectivity, accompanied by network hyperexcitability and hypersynchronicity. These findings support inhibitory-neuron-specific mechanisms in mediating the epileptogenic effects of KCNT1 channel GOF, offering cell-type-specific currents and effects as promising targets for therapeutic intervention.

INTRODUCTION

K^+ channels play essential roles in regulating the membrane excitability of neurons, and their dysfunction causes a wide range of neurological diseases, particularly epilepsy (Köhling and Wolfart, 2016; Villa and Combi, 2016; Oyrer et al., 2018). Traditionally, this mechanism has been conceptualized as loss-of-function (LOF) variants decreasing K^+ currents and leading to neuronal hyperexcitability. Recent human gene discovery efforts, however, have identified novel, neurological-disease-associated K^+ channel variants that increase peak K^+ current magnitudes when expressed in heterologous cells, suggesting that they are gain-of-function (GOF) variants (Yang et al., 2013; Syrbe et al., 2015; Simons et al., 2015; Millichap et al., 2017; Du et al., 2005; Miceli et al., 2015; Lee et al., 2014). Although these variants have been biophysically characterized, how they function in neurons and networks to cause hyperexcitability is unknown (Niday and Tzingounis, 2018).

Among K^+ channels, variants in the gene encoding the Na^+-activated K^+ (K_{Na}) channel KCNT1 (Slack, K_{Na} 1.1) cause a range of epilepsies, including early infantile epileptic encephalopathies (EIEEs) (Ohba et al., 2015), malignant migrating partial seizures of infancy (MMPSI) (Barcia et al., 2012), and autosomal dominant nocturnal frontal lobe epilepsy (ADNFLE) (Heron et al., 2012; Møller et al., 2015). These variants increase peak K^+ current magnitude, potentially by increasing the cooperativity (Kim et al., 2014), enhancing the Na^+ sensitivity, increasing the open probability, and/or shifting the voltage dependence of the mutant KCNT1 channel (Tang et al., 2016; McTague et al., 2018). The broad-spectrum K^+ channel blocker quinidine can normalize the increased K^+ currents caused by pathogenic *KCNT1* variants (McTague et al., 2018; Milligan et al., 2014) and thus has been tried as a precision therapy to treat KCNT1-associated neurodevelopmental disease. Although some early cases were promising (Bearden et al., 2014), further reports showed limited therapeutic benefit of quinidine in KCNT1-related epilepsy (Mullen et al.,

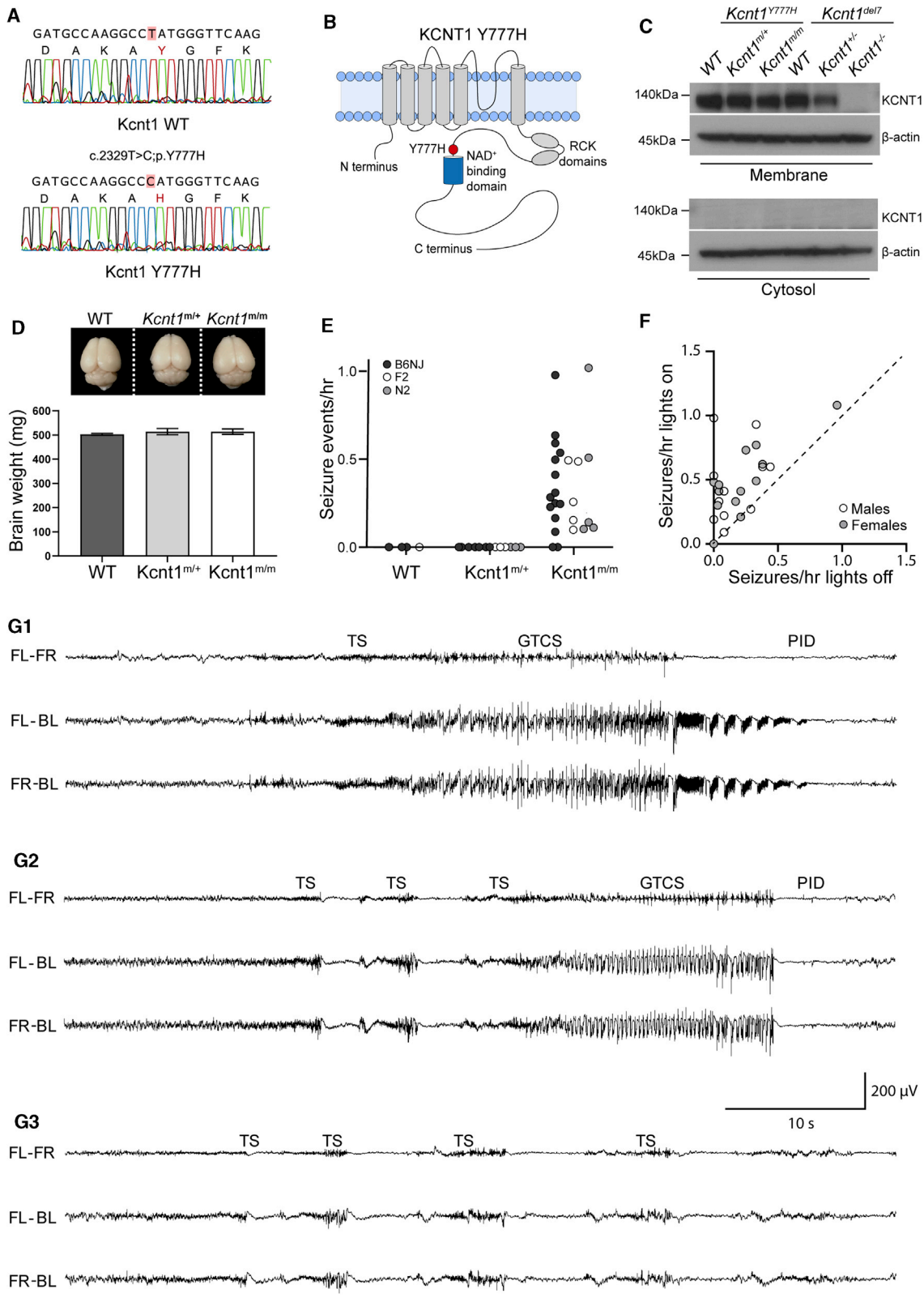

(legend on next page)

2018; Chong et al., 2016; Fitzgerald et al., 2019), emphasizing that an understanding of disease mechanisms beyond channel biophysics is necessary to advance clinical treatment.

In normal neuronal physiology, there is evidence that the K_{Na} current mediated by KCNT1 can activate in three distinct activity regimes: during bursts of action potentials (APs) to reduce neuronal excitability and control interburst timing (Schwindt et al., 1989; Wallén et al., 2007; Kim and McCormick, 1998; Yang et al., 2007), after a single AP to increase afterhyperpolarization (AHP) and enhance bursting (Franceschetti et al., 2003; Liu and Stan Leung, 2004), or at subthreshold voltages to modify intrinsic neuronal excitability (Martinez-Espinosa et al., 2015; Reijntjes et al., 2019; Hage and Salkoff, 2012). The effect of a *KCNT1* GOF variant on neuronal physiology and network activity would therefore depend on which of these regimes were affected. Following this, it has been hypothesized that *KCNT1* GOF variants lead to network hyperexcitability by (1) accelerating AP repolarization selectively in excitatory neurons, thereby limiting sodium channel inactivation and causing a higher AP firing frequency; (2) reducing membrane excitability or inducing spike frequency adaptation selectively in inhibitory neurons, resulting in disinhibition; or (3) causing developmental alterations in synaptic connectivity, thus leading to a hyperexcitable network (Kim and Kaczmarek, 2014; Niday and Tzingounis, 2018; Milligan et al., 2014). To test these hypotheses, we generated a mouse model with a human-disease-causing GOF variant in the *Kcnt1* gene and used a multiplatform approach to identify a time point, brain region, and neuron type that demonstrated strong functional alterations. We found that the *Kcnt1* variant selectively increases K_{Na} currents in inhibitory neurons at subthreshold voltages to reduce their intrinsic excitability and alters synaptic connectivity to promote a hyperexcitable and hypersynchronous network, thus providing a paradigm for how GOF variants in K^+ channels cause neurodevelopmental disease.

RESULTS

The *Kcnt1*-Y777H Mouse Model Exhibits Epileptic and Behavioral Phenotypes Similar to Those of Human Patients

The genetic variant Y796H (c.2386T > C; p.[Tyr796His]) in *KCNT1* has been identified as a heterozygous mutation causing both inherited and *de novo* cases of a severe, early-onset form of ADNFLE (Heron et al., 2012; Mikati et al., 2015). In heterologous systems, the Y796H variant enhances the Na^+ sensitivity of KCNT1 and increases the peak K_{Na} current from 3- to 11-fold over the WT channel (Tang et al., 2016; Milligan et al., 2014). To model this *KCNT1* GOF variant-associated intractable childhood epilepsy in mice, we introduced a missense mutation (c.2329T > C) into the endogenous *Kcnt1* allele on the C57BL/6NJ (B6NJ) strain background (Figure 1A). This mutation encodes a Y777H (p.[Tyr777His]) alteration corresponding to Y796H that lies adjacent to the NAD^+-binding site of KCNT1 (Figure 1B). We generated cohorts of wild-type (WT), heterozygous (*Kcnt1*$^{m/+}$), and homozygous (*Kcnt1*$^{m/m}$) littermates. Genetic transmission of both alleles was normal, and no selective lethality was seen in either mutant genotype at any age. Western blot analysis of membrane and cytosolic protein fractions isolated from the cortices of WT, *Kcnt1*$^{m/+}$, and *Kcnt1*$^{m/m}$ mice detected KCNT1 only in the membrane fraction from WT mice, and importantly, levels and localization of the Y777H variant were unaltered in *Kcnt1*$^{m/+}$ and *Kcnt1*$^{m/m}$ mice (Figure 1C). Finally, dissected brains from 10- to 12-week-old *Kcnt1*$^{m/+}$ and *Kcnt1*$^{m/m}$ mice appeared similar in morphology and size to their WT littermates (Figure 1D), suggesting that expression of the *Kcnt1* GOF variant does not grossly alter brain development.

Patients with KCNT1-associated ADNFLE present with frequent, often nocturnal seizures with a variety of phenotypes, including hypermotor, focal with tonic posturing, and secondary generalized tonic-clonic (Gertler et al., 2018; Mikati et al., 2015; McTague et al., 2018; Fitzgerald et al., 2019). To test for the presence of spontaneous seizures, we monitored adult mice ($\geq$7 weeks of age) of each genotype using video electroencephalography (video-EEG) recordings. Epileptiform activity was not observed in WT (n = 3) or *Kcnt1*$^{m/+}$ (n = 8) mice. However, 87% (13/15) of *Kcnt1*$^{m/m}$ mice had at least one spontaneous seizure in an average of 38 h of continuous recording (Figure 1E, black dots). To test the impact of the *Kcnt1* GOF variant on seizure activity in a broader genetic context, we performed video-EEG on WT, *Kcnt1*$^{m/+}$, and *Kcnt1*$^{m/m}$ mice on a mixed background using an FVB-based partner strain (see STAR Methods). Of the F_2 and N_2 hybrid *Kcnt1*$^{m/m}$ mice, 100% (10/10) had at least one spontaneous seizure in an average of 47 h of continuous recording, whereas seizures were not observed in WT (n = 1) or *Kcnt1*$^{m/+}$ (n = 6) mice (Figure 1E, gray and white dots). Thus, although heterozygous expression of the Y796H variant is sufficient to cause

Figure 1. Homozygous *Kcnt1*-Y777H Mice Have Frequent, Sleep-Associated, Spontaneous Seizures

(A) Sanger sequencing chromatograms show the WT (top) and Y777H (bottom) alleles obtained from direct sequencing of PCR products amplified from genomic DNA from a WT and a *Kcnt1*$^{m/m}$ mouse.

(B) Diagram of the KCNT1 protein shows location of the Y777H residue.

(C) Western blots show KCNT1 expression in *Kcnt1*^{Y777H} (WT, *Kcnt1*$^{m/+}$, and *Kcnt1*$^{m/m}$) P0 cortices following membrane and cytosol fractioning. The corresponding lysates from the *Kcnt1* mouse knockout *Kcnt1*^{del7} (WT, *Kcnt1*$^{+/-}$, and *Kcnt1*$^{-/-}$) were used as a negative control.

(D) Representative image shows similar gross morphology of brains dissected from 10- to 12-week-old WT, *Kcnt1*$^{m/+}$, and *Kcnt1*$^{m/m}$ littermate mice. Bar graph shows that brain weight is unaltered by the Y777H variant (WT; n = 3, *Kcnt1*$^{m/+}$; n = 4, and *Kcnt1*$^{m/m}$; n = 3). Data are represented as mean ± SEM.

(E) Dot plot shows the combined spontaneous generalized tonic-clonic seizure (GTCS) and tonic seizure (TS) frequency in WT, *Kcnt1*$^{m/+}$, and *Kcnt1*$^{m/m}$ mice in three genetic backgrounds indicated by shaded dots.

(F) Scatterplot shows that seizures are more likely to occur when lights are on. Each dot represents one *Kcnt1*$^{m/m}$ mouse and is shaded to indicate sex.

(G_1–G_3) Representative EEG traces show seizure episodes from B6NJ *Kcnt1*$^{m/m}$ mice, including GTCS, TS, epileptiform discharges (EDs), and post-ictal depression (PID) episodes as noted in each panel. The traces shown are differential recordings between front left (FL), front right (FR), and back left (BL) EEG electrodes.

See also Figure S1 and Table S1.

frequent seizures in patients, *Kcnt1*-Y777H heterozygous mice did not exhibit any detectable epileptiform activity. Therefore, we focused the remainder of our study on *Kcnt1*-Y777H homozygous mice to understand the contribution of K^+ channel GOF to seizure disorders.

To determine whether the seizures observed in *Kcnt1*$^{m/m}$ mice recapitulate the signature features of those in KCNT1-associated ADNFLE patients, we analyzed the relationship between seizure activity and sleep in *Kcnt1*$^{m/m}$ mice. Strikingly, regardless of mouse strain or sex, the incidence of seizure episodes was ~2-fold higher when the vivarium lights were on, corresponding to the sleep period of mice (Figure 1F). Moreover, we compared the incidence of seizures in wake, NREM sleep, and REM sleep in seven B6NJ *Kcnt1*$^{m/m}$ mice and found that 90% (131/145) occurred during NREM sleep (Table S1). Next, we analyzed the video-EEG of all *Kcnt1*$^{m/m}$ mice to assess their seizure phenotypes. Two distinct seizure types were observed: generalized tonic-clonic seizures (GTCSs), typically lasting 30–60 s, and tonic seizures (TSs), typically lasting 1–2 s. TSs often preceded GTCSs (Figures 1G_1 and 1G_2), but TSs also occurred without further progression, sometimes as single events but often in clusters of two or more episodes within a few seconds of each other (Figure 1G_3). Together, these data highlight meaningful parallels between pathology observed in the homozygous mouse model and the human disease caused by the *KCNT1* GOF variant, including seizure frequency, brain state-association, and phenotype.

Because *KCNT1* GOF variants are also associated with intellectual disability and psychiatric conditions, including anxiety and attention-deficit hyperactive disorder, we next performed a series of tests to assess the effects of the Y777H variant on mouse behavior. In an open field test, *Kcnt1*$^{m/m}$ mice exhibited a robust hyperactivity phenotype, traveling a further distance compared to WT littermates; however, they were not different from WT on the elevated plus maze (Figures S1A and S1B), indicating hyperactivity without changes in anxiety-like behaviors. *Kcnt1*$^{m/m}$ mice also exhibited decreased freezing behaviors in the contextual and cued fear conditioning tests, without changes in post-shock freezing behavior or acoustic startle responses (Figures S1C and S1D), suggesting learning deficits unconfounded by sensorimotor deficits. As a global indicator of mouse well-being, we examined nest building, which is often reduced in neurodegenerative and psychiatric murine disease models (Jirkof, 2014). Both *Kcnt1*$^{m/m}$ females and males were poor nest builders compared with WT, as assessed using a score of nest quality and the weight of unshredded nesting material (Figure S1E). These data suggest that, in addition to recapitulating the seizure phenotypes, *Kcnt1*$^{m/m}$ mice exhibit several behavioral phenotypes similar to those found in ADNFLE patients.

Widefield Ca^{2+} Imaging Reveals Network Hyperactivity in the Secondary Motor Cortex of *Kcnt1*$^{m/m}$ Mice

To determine which cortical regions were most strongly impacted by the *Kcnt1* variant, we next crossed *Kcnt1*-Y777H mice to the *Snap25*-GCaMP6s line to generate *Kcnt1*$^{m/m}$; *Snap25*$^{G6s/+}$ and *Kcnt1*$^{+/+}$; *Snap25*$^{G6s/+}$ (hereafter referred to as *Kcnt1*$^{m/m}$-G6s and WT-G6s) littermates. We then imaged spontaneous neural activity across the dorsal cortices of awake, head-fixed, behaving *Kcnt1*$^{m/m}$-G6s and WT-G6s adult mice using a custom tandem-lens epifluorescence macroscope (Figure 2A). Both *Kcnt1*$^{m/m}$-G6s and WT-G6s mice exhibited dynamic, spatially complex patterns of spontaneous cortical activity. To quantify this activity, we performed event detection and plotted the width versus prominence profile of all detected events (Figure 2B). In all *Kcnt1*$^{m/m}$-G6s mice (n = 6), there were narrow, large-amplitude calcium events, similar in appearance to previous reports of interictal epileptiform discharges (IEDs) captured using the same technique (Steinmetz et al., 2017, Rossi et al., 2017). Importantly, these events were rarely observed in WT-G6s littermates (n = 5). Across *Kcnt1*$^{m/m}$-G6s mice, these events were consistently localized to the anterior medial cortex (Figure 2C; Video S1), consistent with previous reports of IEDs localized to the anterior medial cortex in human patients carrying the Y796H variant (Mikati et al., 2015). Alignment of the activity maps from *Kcnt1*$^{m/m}$-G6s mice to the Allen Mouse Common Coordinate Framework (Allen Mouse Brain Connectivity Atlas, Wang, 2020) showed that these events localized primarily to the secondary motor cortex region (M2; Figures 2C and S2), suggesting a regional specificity to the interictal hyperexcitability in *Kcnt1*$^{m/m}$ mice.

In Vivo Electrocorticography Shows Early-Onset Cortical Network Hyperactivity in *Kcnt1*$^{m/m}$ Mouse Pups

KCNT1 epileptic encephalopathy is a childhood genetic disease; therefore, we next tested for evidence of epileptiform activity in mouse pups by performing acute, head-fixed, unanesthetized, *in vivo* electrocorticography on a cohort of *Kcnt1*$^{m/m}$ (n = 8) and WT (n = 5) mice at postnatal day 13 (P13) to P15. Of the eight *Kcnt1*$^{m/m}$ pups, three showed definite seizure activity (Figure 3A), and all eight exhibited waveforms consistent with IEDs (Figure 3C). Electrographic seizure patterns consisted of evolving patterns of spike and wave discharges that had restricted spatial distribution across the cortical surface (Figure 3A). These seizures lasted from 10 to 280 s and stopped spontaneously in all cases (Figure 3B). No WT pups exhibited electrographic seizure activity. Identical offline IED detection algorithms were applied to *Kcnt1*$^{m/m}$ and WT pups, with all *Kcnt1*$^{m/m}$ pups demonstrating a higher occurrence rate of IEDs (Figure 3D). These IEDs were focally distributed over the surface of the cortex across *Kcnt1*$^{m/m}$ pups and, similar to the results from widefield Ca^{2+} imaging, were more concentrated in anterior regions of the somatomotor cortex (Figure 3E).

The *Kcnt1*-Y777H Variant Impairs Excitability and AP Generation in Cortical GABAergic, but Nnot Glutamatergic, Neurons

Video-EEG, widefield Ca^{2+} imaging, and *in vivo* electrocorticography all demonstrated hyperexcitable cortical networks in *Kcnt1*$^{m/m}$ mice, starting as early as the second postnatal week. What are the origins of this hyperexcitability? KCNT1 and the associated K_{Na} current have several proposed roles in the regulation of membrane excitability and AP generation, and *KCNT1* is broadly expressed in neurons (Bhattacharjee et al., 2002, 2005; Rizzi et al., 2016), including multiple subtypes of glutamatergic and GABAergic neurons from both human and mouse cortices

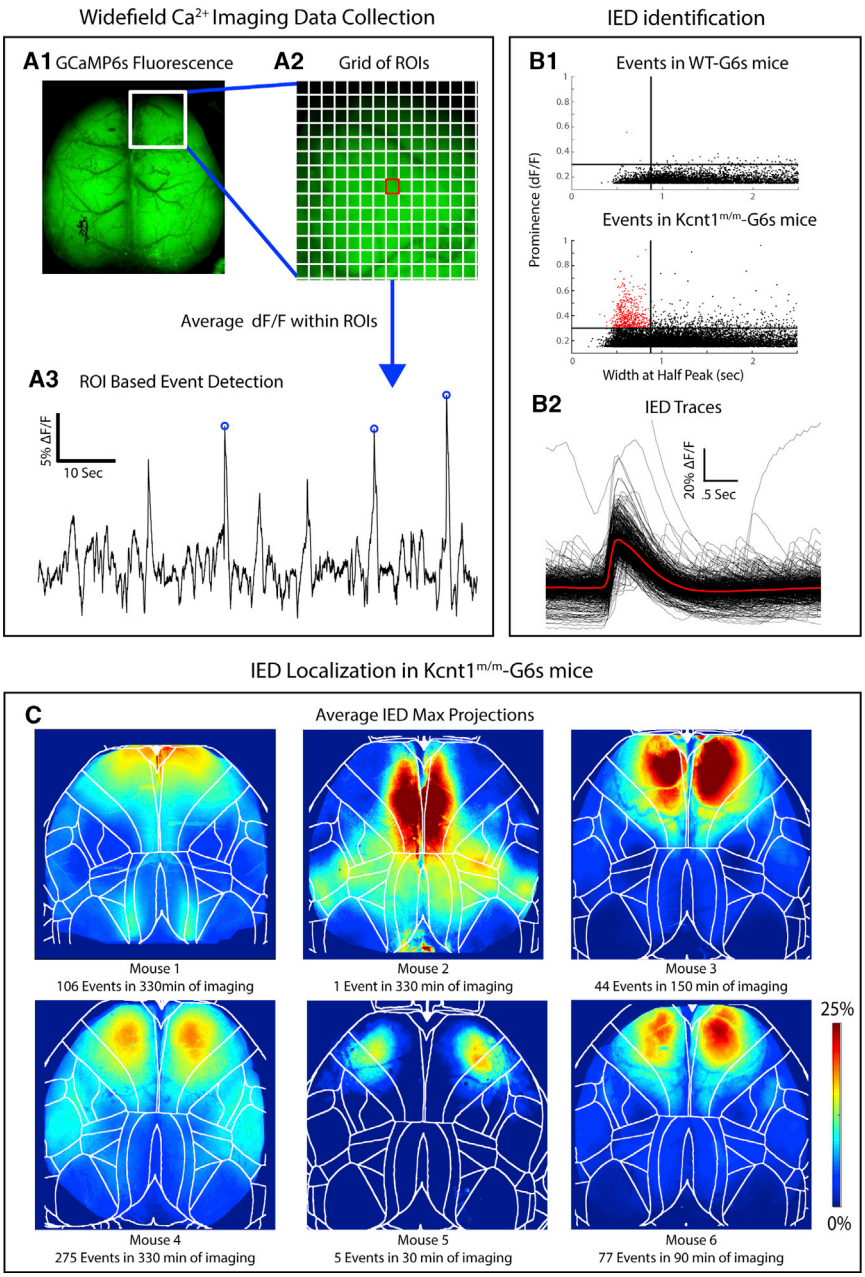

Figure 2. Interictal Epileptiform Discharges (IEDs) in *Kcnt1*$^{m/m}$ Mice Localize to the Secondary Motor Cortex

(A_1) GCaMP6s fluorescence in the brain of a *Kcnt1*$^{m/m}$-G6s mouse. (A_2) Illustration of the grid of regions of interest (ROIs) used in event detection superimposed on a portion of the GCaMP6s fluorescence image. (A_3) ΔF/F peaks with a prominence greater than 15% were identified in each ROI.

(B_1) Maximum event prominence plotted as a function of width at half-maximum for WT-G6s and *Kcnt1*$^{m/m}$-G6s mice. *Kcnt1*$^{m/m}$-G6s mice generate events (narrow, high prominence) not seen in WT-G6s. Lines at 875 ms and 30% ΔF/F indicate our criteria for classifying events as IEDs. (B_2) Overlaid ΔF/F traces of all IEDs in all *Kcnt1*$^{m/m}$-G6s mice with the mean waveform in red. The Kcnt1$^{m/m}$ plot was cropped to highlight the region containing IEDs, which obscures one large event (0.52, 2.17).

(C) To investigate the cortical localization of spike-like events, we generated a maximum projection across all event frames for each IED. The average of these is shown for each *Kcnt1*$^{m/m}$-G6s mouse, showing consistent peak localized to the anterior medial cortex, mostly within primary and secondary motor cortices. Boundaries indicate cortical regions demarcated by aligning brains to the Allen Common Coordinate Framework (CCF) (see STAR Methods).

See also Figure S2 and Video S1.

(Figure S3). Thus, it has been hypothesized that KCNT1 GOF enhances the intrinsic excitability of glutamatergic neurons, or reduces that of GABAergic neurons, to generate a hyperexcitable network. To test these hypotheses, we assessed neuron-subtype-specific effects of KCNT1 GOF on membrane properties and AP firing by performing whole-cell current-clamp analysis of cultured cortical neurons during the time frame of network hyperexcitability onset (days *in vitro* 13 [DIV13] to DIV17). The recorded neurons were classified as glutamatergic, fast-spiking (FS) GABAergic, or non-fast-spiking (NFS) GABAergic, based on expression of GFP driven by the *CaMKII* promoter, AP parameters, and evoked synaptic responses (see STAR Methods).

First, we assessed the membrane excitability of *Kcnt1*$^{m/m}$ glutamatergic neurons. If the K_{Na} current activated at subthreshold voltages in *Kcnt1*$^{m/m}$ neurons, KCNT1 GOF would be expected to alter the resting membrane potential (V_{rest}), input resistance (R_{in}), AP threshold, or the minimum amount of current needed to trigger an AP (rheobase); however, none of these parameters were significantly affected by the Y777H variant in glutamatergic neurons (Table S2; Figures 4A_1 and 4A_2). Alternatively, it has been hypothesized that the K_{Na} current activates in response to AP firing and that KCNT1 GOF increases the rate of AP repolarization in glutamatergic neurons, leading to an increase in AP firing frequency. In this case, KCNT1 GOF would be expected to alter the AP shape; however, the AP half-width, AP repolarization rate, and AHP were also not significantly affected by the Y777H variant (Table S2; Figure 4A_3). Accordingly, the AP firing responses to incremental current injections were also indistinguishable between WT and *Kcnt1*$^{m/m}$ glutamatergic neurons (Figure 4A_4). Thus, despite the reported expression of KCNT1 and K_{Na} currents in cortical glutamatergic neurons (Budelli et al., 2009, Rizzi et al., 2016), there were no significant alterations in any of the electrophysiological parameters measured in this neuron type.

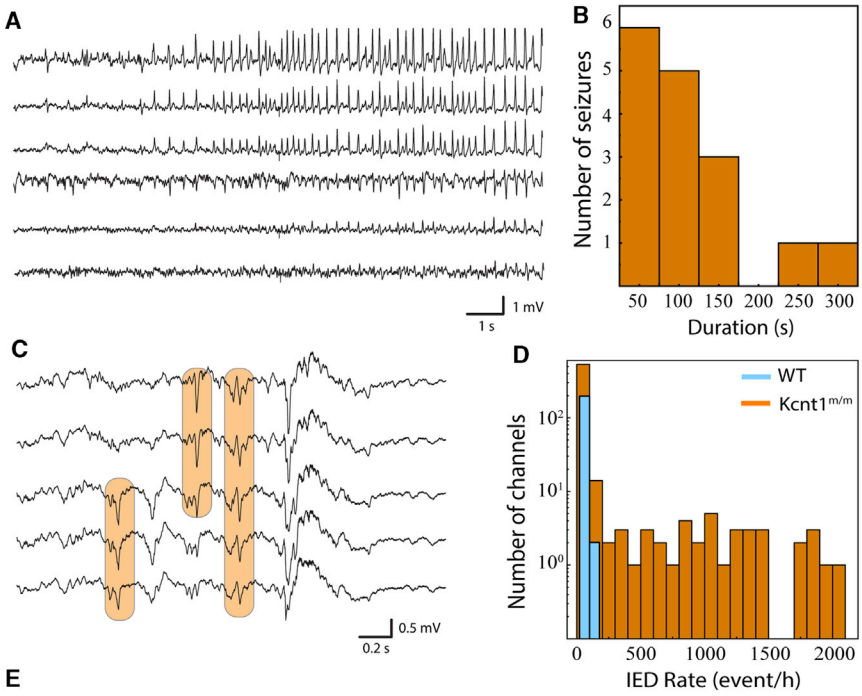

Figure 3. *Kcnt1*$^{m/m}$ Mice Have Epileptic Activity *In Vivo* at 2 Weeks of Age

(A) Sample raw traces from electrocorticography array demonstrate focal, evolving ictal pattern in a head-fixed pup.

(B) Histogram of seizure duration across *Kcnt1*$^{m/m}$ pups. Three out of eight *Kcnt1*$^{m/m}$ pups had definite seizures, and none of the five WT pups had seizures.

(C) Sample raw traces from surface electrocorticography array demonstrate populations of interictal epileptiform discharges (IEDs; orange boxes).

(D) Histogram of IED occurrence across all functioning electrocorticography channels in *Kcnt1*$^{m/m}$ (orange) and WT (blue) pups.

(E) IED occurrence rate localized anatomically across the electrocorticography array and pooled across pups reveals focal distribution in mutants. Each square represents one electrocorticography electrode. The approximate location and scale of the arrays on the dorsal cortical surface is shown at left. Color map is normalized across *Kcnt1*$^{m/m}$ and WT pups.

An alternative hypothesis is that KCNT1 GOF selectively reduces the excitability of GABAergic neurons. Although, like glutamatergic neurons, the *Kcnt1*$^{m/m}$ FS neurons showed no alterations in V_{rest}, R_{in}, or AP threshold, they did show an increase in the rheobase current (Table S2; Figures 4B_1 and 4B_2), suggesting there may be an increased K_{Na} current near AP threshold levels in this neuron population. Other electrophysiological parameters assessed, including AP half-width, AP repolarization rate, and AHP, were not affected by the Y777H variant in FS neurons (Table S2; Figure 4B_3). However, incremental current injections showed a decrease in the number of APs per current step in *Kcnt1*$^{m/m}$ FS neurons relative to that of WT (Figure 4B_4).

In contrast to glutamatergic and FS neurons, the *Kcnt1*$^{m/m}$ NFS neurons showed drastic alterations in membrane properties and AP generation relative to those of WT. The *Kcnt1*$^{m/m}$ NFS neurons showed a decrease in R_{in}, accompanied by a large increase in the rheobase (Figures 4C_1 and 4C_2), whereas the V_{rest} and AP threshold were unchanged (Table S2). The membrane capacitance (C_m) was also increased in *Kcnt1*$^{m/m}$ NFS neurons (Table S2). There were several other alterations to the AP parameters in *Kcnt1*$^{m/m}$ NFS neurons, including a narrower AP half-width, a faster AP repolarization rate, and a larger AHP (Table S2; Figure 4C_3). These data suggest there may be a larger increase in the K_{Na} current in this neuron population or that the K_{Na} current is increased across a wider voltage range. Importantly, incremental current injections showed a strong decrease in the number of APs per current step in *Kcnt1*$^{m/m}$ NFS neurons relative to that of WT (Figure 4C_4). Overall, these data demonstrate that the Y777H variant selectively reduces the intrinsic excitability of FS and, to a greater extent, NFS GABAergic neurons, thus providing a functional answer to the question of how a variant that causes a decrease in excitability could lead to the formation of a hyperexcitable network.

The Y777H Variant Left-Shifts the Voltage-Dependent Activation of KCNT1 and Increases Subthreshold K_{Na} Currents Only in GABAergic Neurons

Why are GABAergic neurons more sensitive to the effects of a variant in a gene that is widely expressed in neurons? To address this question, we recorded K_{Na} currents in cultured cortical neurons by applying voltage steps to voltage-clamped neurons and comparing the delayed outward current before and after the addition of tetrodotoxin (TTX), as KCNT1 channels are thought to be the major contributors to this current (Budelli et al., 2009; Reijntjes et al., 2019; Cervantes et al., 2013). Consistent with KCNT1-mediated currents recorded previously using the same technique, we observed K_{Na} currents in all three WT neuron types, beginning at approximately ~10 mV and increasing with depolarization (Figures 5$A_{1,2}$–5$C_{1,2}$). At more negative potentials, the TTX-sensitive current was often net inward (Figures 5A_3–5C_3), likely due to the persistent Na^+ current (I_{NaP}), which has been shown to prime K_{Na} for activation in some neuron types (Budelli et al., 2009; Hage and Salkoff, 2012).

The Y777H variant altered K_{Na} currents in ways consistent with it being a GOF variant, but the nature of the changes was unique to each neuron type. In all *Kcnt1*$^{m/m}$ neuron types, the overall K_{Na} current was increased, as measured by a significant effect of

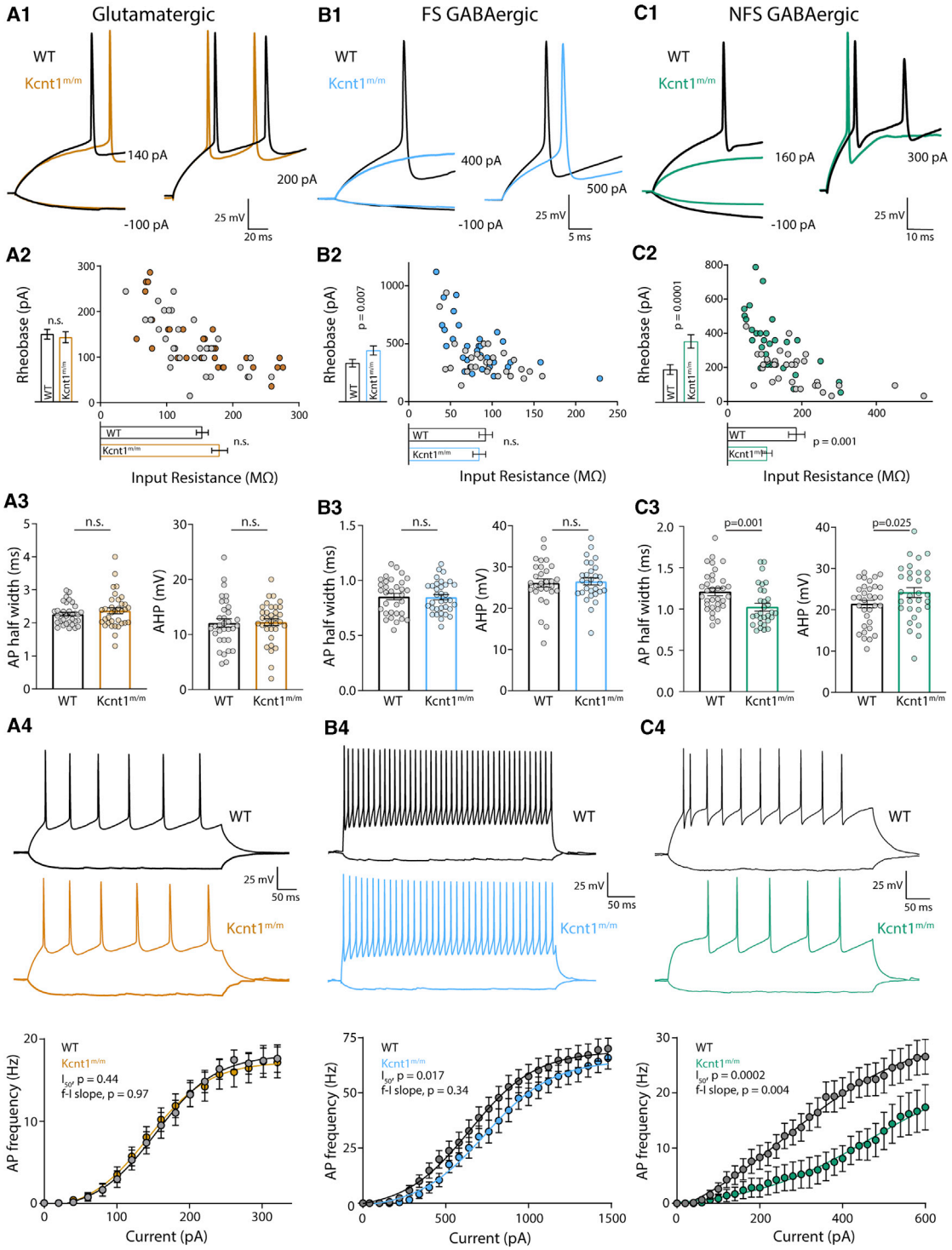

Figure 4. The *Kcnt1* Y777H Variant Causes a Reduction in Membrane Excitability and AP Generation in GABAergic, but Not Glutamatergic, Cortical Neurons

(A_1–C_1) Representative membrane voltage traces of WT (black) and *Kcnt1*$^{m/m}$ (colors) neurons of the indicated type in response to current injections illustrate differences in the input resistance (R_{in}) and/or rheobase between WT and *Kcnt1*$^{m/m}$ GABAergic neurons.

(A_2–C_2) The individual values of R_{in} (x axis) and rheobase (y axis) for WT (gray) and *Kcnt1*$^{m/m}$ (colors) neurons. The mean and SEM for each group are indicated by the bars next to the corresponding axis.

(A_3–C_3) Individual values and mean ± SEM for AP half-widths and AHP in WT (black and gray) and *Kcnt1*$^{m/m}$ (colors) neurons.

(legend continued on next page)

genotype using a linear model, and all showed apparent increases in current at positive potentials compared to those of WT (Figures 5A$_2$–5C$_2$). However, pairwise comparisons at each voltage step showed voltage-dependent differences in current increases among the *Kcnt1*$^{m/m}$ neuron types. For *Kcnt1*$^{m/m}$ glutamatergic neurons, significant increases in the K_{Na} current were only at very depolarized voltages, from +30 to +50 mV (Figure 5A$_2$), whereas the currents at 0 mV and below were indistinguishable from those of WT (Figure 5A$_3$). Conversely, in *Kcnt1*$^{m/m}$ FS neurons, significant increases in K_{Na} currents only occurred at more negative voltage steps, including −50, −40, and −10 mV (Figures 5B$_2$ and 5B$_3$). *Kcnt1*$^{m/m}$ NFS neurons showed the broadest increase in K_{Na} currents, with significant increases at all voltage steps from −60 to +10 mV (Figures 5C$_2$ and 5C$_3$). Plotting the K_{Na} current densities (pA/pF) of NFS neurons showed similar results (Figure S4), suggesting that the increased C_m of *Kcnt1*$^{m/m}$ NFS neurons does not contribute to their increased K_{Na} currents.

To better assess neuron-subtype-specific effects of the Y777H variant on KCNT1 channel function, we plotted the mean normalized conductances of WT and *Kcnt1*$^{m/m}$ neurons as a function of voltage (activation curves). For glutamatergic neurons, the activation curves were not different between the two genotypes, as indicated by their similar membrane potential at half-maximum (V_{50}) values (WT: 16.5 ± 1.0 mV, *Kcnt1*$^{m/m}$: 15.8 ± 0.6 mV, p = 0.54; Figure 5A$_4$). These data, together with the overlapping K_{Na} currents observed throughout the subthreshold voltage range in WT and *Kcnt1*$^{m/m}$ glutamatergic neurons, are consistent with the unaltered membrane properties of *Kcnt1*$^{m/m}$ glutamatergic neurons. However, for FS and NFS GABAergic neurons, the activation curves were significantly left-shifted by the Y777H variant, as evidenced by a 6.5-mV (WT: 12.1 ± 1.2 mV, *Kcnt1*$^{m/m}$: 5.6 ± 1.4 mV, p = 0.0005; Figure 5B$_4$) and 6.3-mV (WT: 15.7 ± 0.8 mV, *Kcnt1*$^{m/m}$: 9.4 ± 0.8 mV, p < 0.0001; Figure 5C$_4$) decrease in V_{50}, respectively. These strong GABAergic-specific left shifts in the voltage-dependent activation of the KCNT1-Y777H channel likely contribute to the increases in K_{Na} currents at subthreshold membrane potentials, and the increases in rheobase and decreases in AP firing, that were observed in the FS and NFS neurons.

Glutamatergic neurons showed large increases in the K_{Na} current at depolarized voltages but no effects on membrane excitability, whereas GABAergic neurons, especially NFS, showed smaller absolute increases but large effects on membrane excitability. Reasoning that the effect of the altered K_{Na} current on membrane excitability would depend on how much it increased the total membrane current (I_m), we plotted I_m across all voltage steps for each neuron type, WT and *Kcnt1*$^{m/m}$ (Figures 5A$_5$–5C$_5$), as well as the fractional increase in I_m caused by the variant (ΔI/I; Figures 5A$_5$–5C$_5$, lower panels). In glutamatergic neurons, the maximal ΔI/I was from +20 to +50 mV, where *Kcnt1*$^{m/m}$ neurons had a ∼20% increase compared to WT. In FS *Kcnt1*$^{m/m}$ neurons, the maximum ΔI/I was ∼30%, which occurred from −10 to +30 mV. In NFS *Kcnt1*$^{m/m}$ neurons, the ΔI/I was 50%–60% throughout the subthreshold voltages, reaching values as high as 65% at −20 mV. These results are consistent with the observed neuron-subtype-specific effects of the *Kcnt1* GOF variant, with the smallest fractional increase in the K^+ current occurring in glutamatergic neurons and the largest in NFS neurons; more specifically, the large increase in ΔI/I across subthreshold voltages in *Kcnt1*$^{m/m}$ NFS neurons predict the robust effects observed on membrane excitability, including the decreased R_{in}, increased rheobase, and impaired AP firing.

To provide further evidence for the specificity of the K_{Na} current increases and their relationship to membrane excitability, we recorded K_{Na} currents and assessed alterations in membrane excitability in neurons with heterozygous expression of the Y777H variant (Figure S5). Heterozygous expression of Y777H increased K_{Na} currents in the same voltage ranges as homozygous expression in all three neuron types, and with current magnitudes intermediate to those seen in corresponding WT and homozygous neurons, demonstrating a gene dosage effect of the *Kcnt1*-Y777H variant on K_{Na} current increases. Furthermore, NFS neurons with heterozygous expression of Y777H showed an intermediate increase in rheobase current compared with those of WT and homozygous neurons, suggesting a tight relationship between the increase in K_{Na} current at subthreshold voltages and the deficit in AP generation in NFS neurons.

The *Kcnt1*-Y777H Variant Increases Homotypic Synaptic Connectivity and Induces a Hyperexcitable and Hypersynchronous Network

Our finding that KCNT1 GOF caused a selective reduction in GABAergic neuron excitability is not mutually exclusive with the third proposed hypothesis, which is that *KCNT1* GOF variants cause network excitability because increases in K^+ current during development alter normal patterns of synaptic connections (Kim and Kaczmarek, 2014). Thus, we tested for altered synaptic connectivity by performing paired recordings of glutamatergic (excitatory [E]) and GABAergic (inhibitory [I]) neurons and alternatively stimulating each neuron at 0.1 Hz to test baseline connection probability (P_c) and strength at the four possible motifs (I-I, I-E, E-I, and E-E). P_c at the I-E and E-I motifs was not altered in *Kcnt1*$^{m/m}$ networks (Figures 6B and 6C), indicating grossly normal synaptic interactions between glutamatergic and GABAergic neurons. However, P_c between both I-I and E-E pairs was higher in *Kcnt1*$^{m/m}$ networks than in those of WT (Figures 6A and 6D). The amplitudes of the evoked postsynaptic currents (ePSCs) between connected neurons was not significantly different between genotypes for any of the four connection types (Figures 6A–6D). Thus, in addition to impairing the excitability of GABAergic neurons, the Y777H variant increased synaptic connectivity in the network in ways that should, theoretically, further enhance excitation (increased E-E connections) and reduce inhibition (increased I-I connections).

(A$_4$–C$_4$) Example traces and summary data showing the number of APs (mean and SEM) per current injection step in WT (black and gray) and *Kcnt1*$^{m/m}$ (colors) neurons. The lines in the current/AP plots are fits to a Boltzmann sigmoidal curve and were used to determine the half-max current (I_{50}) and the frequency-current (f-I) slope for each group. Statistical significance was tested using generalized linear mixed models.
See also Figure S3 and Table S2.

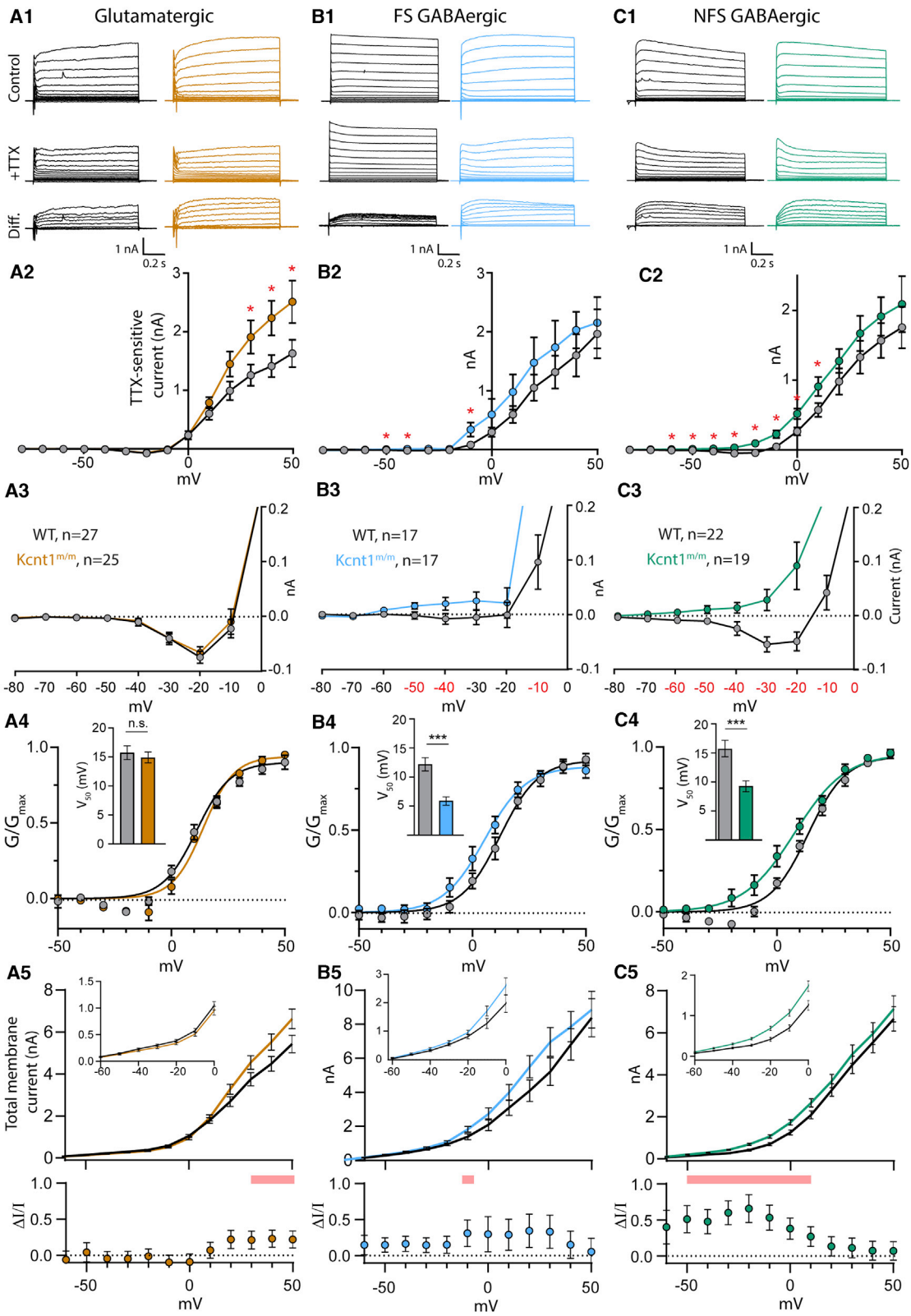

(legend on next page)

To determine whether the increases in synaptic connectivity were accompanied by alterations in synaptic activity, we recorded spontaneous postsynaptic currents (sPSCs; spontaneous excitatory postsynaptic currents [sEPSCs] and spontaneous inhibitory postsynaptic currents [sIPSCs]) onto voltage-clamped glutamatergic and GABAergic neurons. Similar to the increase in E-E synaptic connectivity, we observed an increase in sEPSC frequency onto *Kcnt1*$^{m/m}$ glutamatergic neurons (Figure 6E). Interestingly, although sEPSC frequency was not altered onto the *Kcnt1*$^{m/m}$ GABAergic neuron population as a whole, it was increased onto those with an NFS phenotype, suggesting there may be a compensatory increase in excitatory drive onto *Kcnt1*$^{m/m}$ NFS neurons (Figure S6). This increased excitatory drive may offset the effects of the decreased membrane excitability of these neurons, as sIPSCs were not significantly affected onto *Kcnt1*$^{m/m}$ glutamatergic or GABAergic neurons (Figure 6F). Moreover, in agreement with the ePSC measurements, the amplitudes and kinetics of the sPSCs were not different between the genotypes onto either neuron group (Table S3). Finally, to assess the net effect of altered sPSC activity onto *Kcnt1*$^{m/m}$ neurons, we calculated the E/I ratio, taking into account the relative frequency and size of the sPSCs. E/I ratio onto *Kcnt1*$^{m/m}$ glutamatergic neurons was significantly higher than that onto WT, whereas the E/I ratio onto GABAergic neurons was similar between the two groups (Figure 6G). Thus, the overall balance of excitation and inhibition in *in vitro Kcnt1*$^{m/m}$ networks is shifted toward excitation.

Finally, we tested whether *in vitro* networks of *Kcnt1*$^{m/m}$ neurons exhibit hyperexcitable and/or hypersynchronous behavior, effects that would be predicted downstream of the GABAergic impairments, increased homotypic synaptic connectivity, and altered E/I ratio. To assess these network behaviors, we made primary cultures of cortical neurons from *Kcnt1*$^{m/m}$ and WT P0 pups and recorded spontaneous spiking activity using multi-electrode array (MEA) analysis. We analyzed a variety of spiking and bursting features between DIV9 and DIV27 (see STAR Methods). Networks of *Kcnt1*$^{m/m}$ and WT neurons matured at a similar rate, as measured by the increase in the number of active electrodes (nAEs) per well, which reached a maximum by DIV17 (not shown), and displayed a variety of activity patterns (Figure 6H). In networks of *Kcnt1*$^{m/m}$ neurons, we observed a hyperexcitability phenotype, characterized by an increased mean firing rate (MFR) and an increased bursting frequency (increase in bursts/minute and decrease in interburst interval) (Figure 6I). We also observed an increase in synchrony at the network level, characterized by an increased number of network bursts (Figure 6I). Together, these data suggest that KCNT1 GOF alters intrinsic GABAergic excitability and synaptic connectivity to promote a hyperexcitable and hypersynchronous network.

Acute Cortical Slice Recordings Confirm the Reduced Intrinsic Excitability of *Kcnt1*$^{m/m}$ NFS GABAergic Neurons

Having identified a brain region (Figures 2 and 3) and a neuron type (Figures 4 and 5) that were particularly sensitive to the *Kcnt1* variant, we next wanted to test whether the physiological changes observed in cortical neuron cultures are also present in acute slice, an experimental preparation with a more organized network. We first performed Nissl staining of multiple, coronal 40-μm sections, each containing portions of motor cortex (Figure 7A), from P28 WT and *Kcnt1*$^{m/m}$ littermates to examine potential effects of the *Kcnt1* GOF variant on general cortical structure and lamination. Overall, the brain structures between WT and *Kcnt1*$^{m/m}$ mice appeared highly similar, and the cortical regions in brains of *Kcnt1*$^{m/m}$ mice showed grossly normal cortical thickness and lamination.

We next prepared acute slices containing the anterior motor cortex from P20 to P29 WT and *Kcnt1*$^{m/m}$ mice and performed whole-cell recordings from pyramidal neurons (Figure 7B) and GABAergic neurons (Figure 7F) in the medial portion of the slice. Because more superficial cortical layers are enriched for NFS neurons (Tremblay et al., 2016; Lee et al., 2010) and have been reported to show higher levels of KCNT1 expression (Rizzi et al., 2016), we current-clamped neurons in layer 2/3 and injected steps to elicit APs (Figures 7C and 7G). Similar to observations in cortical neuron cultures, *Kcnt1*$^{m/m}$ glutamatergic neurons showed no changes in R_{in} or rheobase relative to those of WT (Figure 7D). They did, however, have a more depolarized AP threshold (Table S4), an effect that is notably opposite of that previously reported from *Kcnt1* knockout mouse models (Martinez-Espinosa et al., 2015; Reijntjes et al., 2019). Despite their depolarized AP threshold, *Kcnt1*$^{m/m}$ glutamatergic neurons showed AP firing patterns similar to those of WT glutamatergic neurons (Figure 7E).

Importantly, *Kcnt1*$^{m/m}$ NFS neurons showed a significant reduction in R_{in} and large increases in rheobase (Figure 7H) and C_m (Table S4), all of which were changed in the same manner in cultured neurons, although the AP half-width and AHP were

Figure 5. The Y777H Variant Causes Cell-Type-Specific Increases in K_{Na} Currents

(A_1–C_1) Representative traces in control external solution (top), 0.5 μM TTX (middle), and the difference current (bottom), which was calculated by subtracting the membrane current response to voltage steps (−80 to +50 mV) in TTX from the response in control, in WT (black) and *Kcnt1*$^{m/m}$ (colors) neurons.

(A_2–C_2) Summary data show the K_{Na} current (mean ± SEM) for each voltage step in WT (black and gray) and *Kcnt1*$^{m/m}$ (colors) neurons.

(A_3–C_3) Plots of the K_{Na} current (mean ± SEM) for each voltage step from −80 to 0 mV in WT (black and gray) and *Kcnt1*$^{m/m}$ (colors) neurons to illustrate the values that are too small to be seen on the graphs in A_2-C_2.

(A_4–C_4) Normalized Conductance-Voltage (G-V)plots (mean ± SEM) for WT (black and gray) and *Kcnt1*$^{m/m}$ (colors) neurons with Boltzmann fits. Insets show the V_m at half-maximum (V_{50}; mean ± SEM).

(A_5–C_5) Plots of the total membrane current (mean and SEM) for each voltage step from −60 to +50 mV in WT (black) and *Kcnt1*$^{m/m}$ (colors) neurons. Insets show values too small to be seen on the larger graph. Shaded red areas indicate significantly higher currents in *Kcnt1*$^{m/m}$ neurons. The plots below show the fractional increase in the total membrane current (ΔI/I, mean ± SEM) caused by the Y777H variant. Statistical significance for Current-Voltage (I-V) plots was tested using generalized linear mixed models with genotype and current step as fixed effects followed by pairwise comparisons at each level.

p values < 0.05 are labeled on the plots in A_2–C_2 as asterisks and on the plots in A_3–C_3 as red numbers. p values < 0.001 are labeled on the plots in A_4–C_4 as three asterisks. See also Figures S4 and S5.

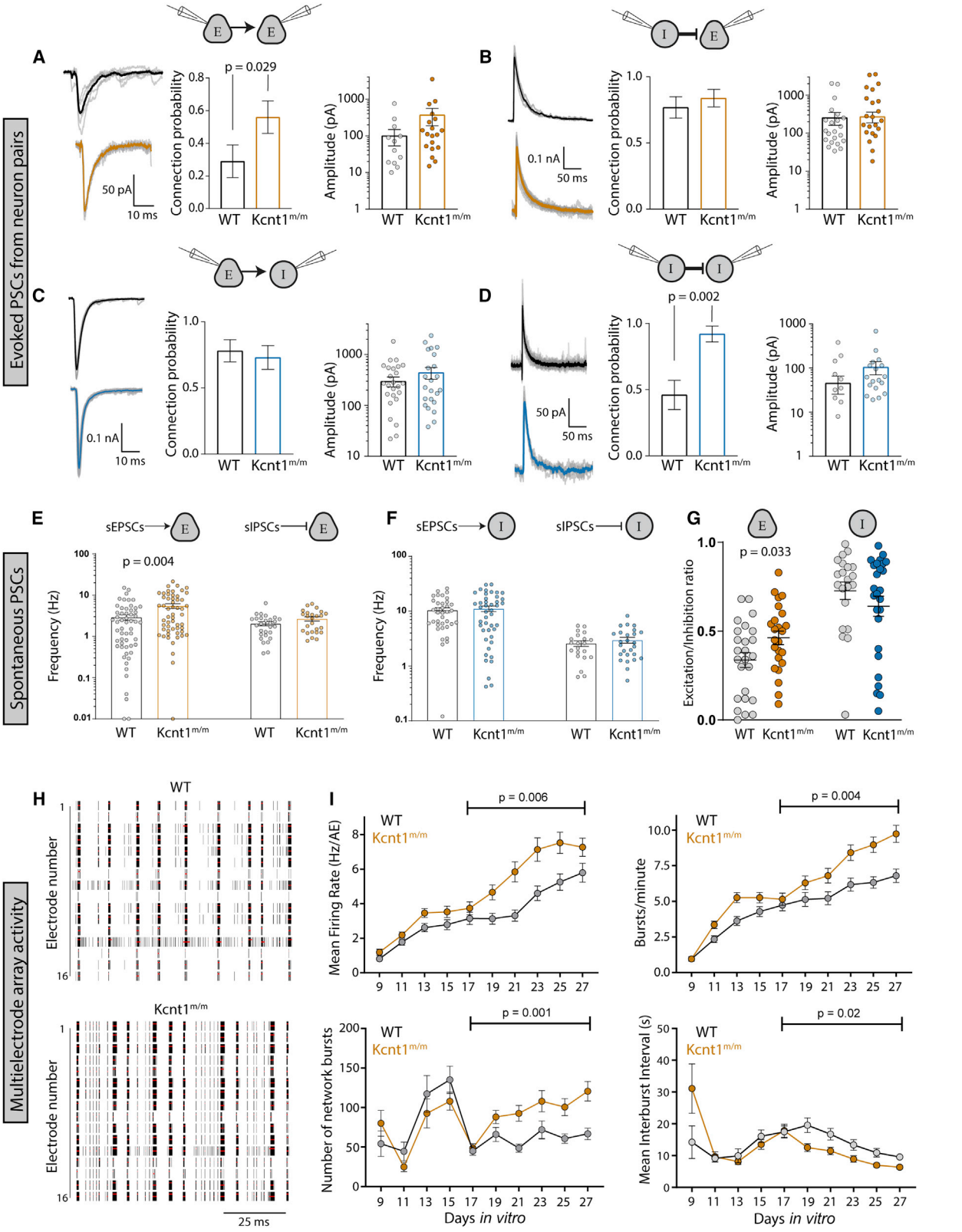

(legend on next page)

unchanged (Table S4). Moreover, incremental current injections demonstrated significant impairments in AP generation in NFS neurons expressing the Y777H variant (Figure 7I). Thus, the main finding from culture, that NFS neurons are most strongly affected by the *Kcnt1*-Y777H variant, was verified in acute slices made from a brain area with demonstrated pathology.

DISCUSSION

Classic and recent human genetic studies have provided key insights into the causes of neurodevelopmental disease and severe epilepsies, revealing that genetic variants in ion channels, both ligand and voltage gated, comprise approximately one-third of known monogenic causes of seizure disorders (Noebels, 2017). Despite the fact that molecular dysfunction of these channel variants is relatively well modeled and correctable in heterologous systems, translating these findings to therapies has faced unexpected challenges, likely due to the developmental, cellular, and synaptic complexity of the brain. Progress in tracing the critical steps between ion channel biophysics and pathological synchronization of cortical neurons thus requires precision genetic disease models and multi-level interrogations of their effects (Oyrer et al., 2018; Farrell et al., 2019).

To address this, we created a mouse model with a missense mutation in a K_{Na} channel gene orthologous to a human missense mutation that causes an early-onset seizure disorder (ADNFLE). Homozygous expression of this GOF variant caused an epileptic phenotype with strong parallels to the human disease, and electrocorticography analysis showed epileptiform activity in *Kcnt1*$^{m/m}$ mice by P14. Early childhood seizures are a common feature of KCNT1-associated (and numerous other) genetic epilepsies, but seizure phenotyping is rarely done at this age in rodents, even though early phenotyping has the potential to uncover seizure phenotypes not present in adults (Lozovaya et al., 2014) and improve our understanding of how well genetic models recapitulate human diseases. Likewise, wide-field Ca^{2+} imaging pinpointed the M2 region as the cortical source of IEDs. These results do not rule out the involvement of other cortical areas in seizure generation or speak to the strong possibility that cortical interactions with subcortical structures are critical for seizure generation. In fact, the finding that seizures in our model are most likely to happen during NREM sleep, coupled with the fact that ADNFLE is also caused by variants in genes that encode nicotinic acetylcholine receptor subunits (Phillips et al., 1995; Sutor and Zolles, 2001), suggests that thalamic input or cholinergic transmission may play a key role in seizure generation (Klaassen et al., 2006).

The multiplatform, *in vivo* phenotyping of the KCNT1 GOF mouse model focused our cellular studies on a discrete time and place. Results from these *in vitro* and *ex vivo* studies support a model in which the *Kcnt1*-Y777H variant increases the K_{Na} current over different voltage ranges in the three major neuron types of the cerebral cortex; glutamatergic, FS GABAergic, and NFS GABAergic. In GABAergic neurons, because it occurs at subthreshold voltages, the K_{Na} current increase impairs membrane excitability and AP generation, changes that are especially strong in the NFS neurons. The reduced excitability of GABAergic neurons is accompanied by increases in E-E and I-I synaptic connectivity, and together, these alterations likely interact to promote both hyperactivity and hypersynchrony in the cortical circuits, especially in cortical region M2, which leads to epileptiform discharges and seizures. This model provides a strong framework for understanding how GOF variants in *KCNT1* lead to epilepsy; however, it remains to be seen if this model will generalize to other GOF variants in K^+ channels, or even other variants within the *KCNT1* gene.

Prior to this study, two other studies were published characterizing *KCNT1* GOF variants, both of which are associated with MMPSI, an earlier onset and more severe form of epilepsy than ADNFLE. Using a knockin mouse model, Quraishi et al. showed that heterozygous expression of the *Kcnt1*-R455H variant results in spontaneous seizure activity in four out of seven mice (Quraishi et al., 2020). However, there were no reports of the effects of the R455H variant on K_{Na} currents or neuronal physiology, making it difficult to compare with mechanistic data from our model. In the other study, homozygous expression of the P942L variant in human induced pluripotent stem cell (iPSC)-derived neurons increases the K_{Na} current, but only at voltages above +40 mV (Quraishi et al., 2019). Similar to our data, they reported a decrease in AP width and increase in AHP; however, in contrast to our data, the P942L variant increases the peak AP firing rate in what are presumably immature glutamatergic neurons. This discrepancy in AP generation identified downstream of the Y796H and P942L variants may be

Figure 6. Increases in Synaptic Connectivity in *Kcnt1*$^{m/m}$ Networks Contribute to Hyperexcitability and Hypersynchrony

(A–D) Evoked postsynaptic currents (PSCs) recorded from neuron pairs (glutamatergic [excitatory (E)] and GABAergic [inhibitory (I)]) by stimulating the neuron type indicated on the left and recording the response in the neuron type indicated on the right (WT, black; *Kcnt1*$^{m/m}$ E, orange; *Kcnt1*$^{m/m}$ I, blue). Left: example traces of evoked ePSCs. Middle: summary data (mean ± SEM) of the connection probability (P_c) between motifs. Right: individual pair values and mean ± SEM of peak evoked PSC amplitudes of connected pairs.

(E) Individual values and mean ± SEM of the spontaneous excitatory postsynaptic current (sEPSC) or inhibitory postsynaptic current (sIPSC) frequency onto excitatory neurons (WT, black; *Kcnt1*$^{m/m}$, orange).

(F) Individual values and mean ± SEM of the sEPSC or sIPSC frequency onto inhibitory neurons (WT, black; *Kcnt1*$^{m/m}$, blue).

(G) The E/I ratio onto excitatory neurons, but not inhibitory neurons, is increased. Individual values and mean ± SEM of the E/I ratios are shown.

(H) Raster plots of multi-electrode array (MEA) data showing WT and *Kcnt1*$^{m/m}$ cortical network firing across the 16 electrodes of a well of a representative plate at DIV23. The black bars indicate spikes, and the red bars indicate bursts.

(I) Graphs plotting measures of spontaneous activity as a function of DIV on MEAs of WT (gray, n = 65 wells, 5 mice) and *Kcnt1*$^{m/m}$ (orange, n = 66 wells, 5 mice) cortical neurons. Mean firing rate (MFR) per active electrodes, number of bursts per minute, number of network bursts, and interburst interval are each shown as the mean ± SEM. Permutated p values for mature DIV17 to DIV27 neurons calculated with a Mann-Whitney *U* test followed by 1,000 permutations are indicated on the graphs.

See also Figure S6 and Table S3.

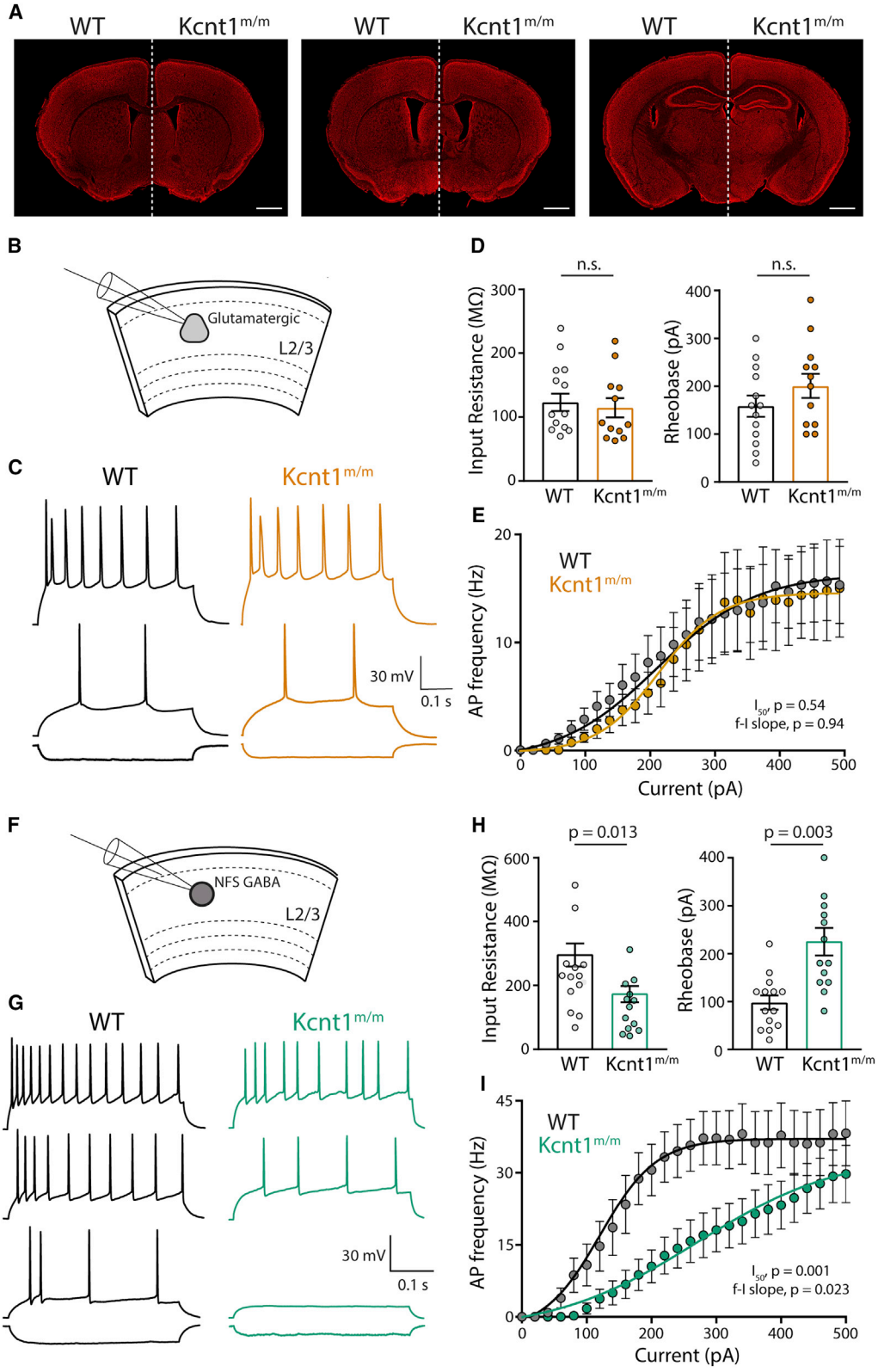

(legend on next page)

because the KCNT1 GOF mechanism is variant and/or disease dependent. Alternatively, we also observed an increased K_{Na} current at suprathreshold voltages in *Kcnt1*$^{m/m}$ glutamatergic neurons. Thus, it is possible that early effects in cortical glutamatergic neuron excitability have resolved by the time we performed our electrophysiology on more mature glutamatergic neurons but could contribute to our observed increase in E-E connectivity (Figure 6A). Future mechanistic studies using knockin mouse models of additional *KCNT1* GOF variants should help resolve these discrepancies and clarify the generality of our findings.

A caveat of our mouse model is that although a heterozygous GOF mutation in *KCNT1* is sufficient to cause ADNFLE in humans, we only detected seizures in homozygous mice. Unfortunately, this caveat is not unique to our model, as several attempts to generate mouse models of heterozygous LOF mutations in K^+ channel genes associated with epilepsy in humans have failed to result in a seizure phenotype in the heterozygous state in mice (Oyrer et al., 2018). Nevertheless, some of these models in the homozygous state, such as *Kcna1* null mice and knockin LOF *Kcnq2* and *Kcnq3* mice, display seizure phenotypes highly similar to those of human patients (Smart et al., 1998; Glasscock et al., 2010; Singh et al., 2008) and have been used successfully to model the human disease and initiate therapeutic studies (Fenoglio-Simeone et al., 2009; Roundtree et al., 2016). Similarly, the strong parallels observed in both the behavior and seizure phenotypes between the homozygous Y777H mouse model and the Y796H-associated disease suggest analogous underlying mechanisms and indicate that the homozygous Y777H mice are a valid preclinical model. Moreover, during the preparation and review of this article, we observed seizures in two *Kcnt1*-Y777H heterozygous mice, one during a widefield Ca^{2+} imaging experiment and the other during a video-EEG experiment. Thus, heterozygous expression can result in seizures in a rodent model, but apparently at a much lower frequency than that observed with homozygous expression, and studies are ongoing to further characterize the heterozygous *Kcnt1*-Y777H phenotype.

A somewhat perplexing finding from our study was that the decreased excitability of *Kcnt1*$^{m/m}$ GABAergic neurons did not lead to decreased sIPSC frequency onto cultured cortical glutamatergic or GABAergic neurons; however, there are several potential explanations for this inconsistency. First, the large literature on Dravet syndrome (DS), another childhood epilepsy disorder, has demonstrated that LOF mutations in the Na^+ channel gene *Scn1a* decrease the excitability of inhibitory neurons. Despite this consensus, electrophysiological recordings in slices have sometimes failed to find reductions in sIPSC frequencies (De Stasi et al., 2016), especially when *Scn1a* deletion is restricted to NFS GABAergic neurons (Rubinstein et al., 2015), which is likely due to the fact that a large portion of NFS GABAergic neurons target the distal dendrites of neurons, far from where sIPSCs are measured at the soma. Moreover, *in vivo* studies of DS models have not shown a decrease in GABAergic neuron firing rates (De Stasi et al., 2016; Tran et al., 2020), even though SCN1A loss causes a more severe phenotype in mice than KCNT1 GOF in our model. Finally, in this study, we also provided experimental evidence that sEPSC frequency onto *Kcnt1*$^{m/m}$ NFS GABAergic neurons is increased (Figure 6H), which likely compensates for their reduced membrane excitability and normalizes sIPSC frequency. Thus, the lack of a decrease in sIPSC frequency is not strong evidence against the hypothesis that inhibitory neuron dysfunction due to KCNT1 GOF contributes to epilepsy.

Kcnt1 mRNA and protein expression in the CNS are thought to be widespread and present in both glutamatergic and GABAergic neurons, indicating that the differential effects we found in these neuron populations are likely not due to selective expression of KCNT1 (Figure S3). In support of this, we found that the Y777H variant increases K_{Na} current in all neuron types analyzed; however, the voltage dependence of these increased currents in each neuron type resulted in drastically different effects on neuronal physiology. In cortical glutamatergic neurons, the K_{Na} current was increased in the +30 to +50 mV range, but the effects of this increase on physiology were extremely limited. This lack of an effect may be due to the fact that in normal physiology, neurons only reach these voltages (30–50 mV) at the peak of the AP and remain there for less than a millisecond, which may not allow for activation of K_{Na}, as the time constant for full activation of KCNT1 channels has been estimated at 25–60 ms (Joiner et al., 1998; Chen et al., 2009). Moreover, the K_{Na} current was increased at negative potentials in both *Kcnt1*$^{m/m}$ GABAergic neuron types, but not in *Kcnt1*$^{m/m}$ glutamatergic neurons. The reasons for the lack of a K_{Na} current increase at subthreshold

Figure 7. NFS GABAergic Neurons in Layer 2/3 of Acute Slices from Motor Cortex of *Kcnt1*$^{m/m}$ Mice Show a Strong Impairment in AP Generation

(A) Representative images of 10-week-old, Nissl-stained coronal sections at three matched bregma levels from WT (left) and *Kcnt1*$^{m/m}$ (right) mice. Scale bar, 1 mm.

(B) Schematic shows the experimental approach of recording glutamatergic neurons in layer 2/3 of the motor cortex.

(C) Representative membrane voltage traces of glutamatergic WT (black) and *Kcnt1*$^{m/m}$ (orange) neurons in response to −100, +140, and +240 pA current injections.

(D) Individual neuron values, mean, and SEM of the R_{in} and rheobase of WT and *Kcnt1*$^{m/m}$ glutamatergic neurons.

(E) Number of APs (mean ± SEM) per current injection step in WT and *Kcnt1*$^{m/m}$ glutamatergic neurons.

(F) Schematic shows the experimental approach of recording NFS GABAergic neurons in layer 2/3 of the motor cortex.

(G) Representative membrane voltage traces of NFS GABAergic WT (black) and *Kcnt1*$^{m/m}$ (green) neurons in response to −100, +100, +180, and +300 pA current injections.

(H) Individual neuron values, mean, and SEM of the R_{in} and rheobase of WT and *Kcnt1*$^{m/m}$ NFS GABAergic neurons.

(I) Number of APs (mean ± SEM) per current injection step in WT and *Kcnt1*$^{m/m}$ NFS GABAergic neurons. The lines in the current/AP plots are fits to a Boltzmann sigmoidal curve that were used to determine the I_{50}. Statistical significance was tested using generalized linear mixed models.

See also Table S4.

voltages in glutamatergic neurons will require further study; however, candidate mechanisms include glutamatergic-specific expression of alternative splice forms of KCNT1, which have been shown to have different activation kinetics, and coexpression of other channels, such as KCNT2, which can form heteromers with KCNT1 and alter its biophysical properties (Chen et al., 2009; Joiner et al., 1998), thus protecting glutamatergic neurons from the more severe effects of KCNT1 GOF.

In GABAergic neurons, we observed the strongest effects of the Y777H variant on K_{Na} currents at voltages between −60 and +10 mV. The role of the K_{Na} current in neurons, at subthreshold voltages in particular, has been controversial, largely because early studies suggested that the Na^+ concentration needed to activate K_{Na} was higher than that normally found in neurons. However, recent studies have shown that K_{Na} can be activated by a persistent Na^+ (Na_P) current present at voltages as low as −90 mV (Hage and Salkoff, 2012). Consistent with this subthreshold role for KCNT1, multiple studies have shown that mouse sensory neurons lacking a K_{Na} current, due to *Kcnt1* knockout, have no alterations in AHP or AP repolarization but instead show decreases in AP threshold and rheobase and increases in AP firing (Martinez-Espinosa et al., 2015; Reijntjes et al., 2019; Lu et al., 2015). These KCNT1 LOF effects on neuronal physiology nicely complement our GOF effects, and taken together, these data support a central role for KCNT1-mediated currents in regulating neuronal excitability at subthreshold potentials.

Among GABAergic neurons, we identified strong KCNT1 GOF effects on the NFS subtype, which are still electrically, molecularly, and morphologically diverse, with subclasses performing distinct roles in circuit function (Markram et al., 2015). The similar, yet more subtle, effects on the FS subtype suggest that there is likely not one particular subclass of inhibitory neurons that is uniquely affected. What cell type differences could account for the stronger effects of KCNT1 GOF on NFS than FS GABAergic neurons? First, as proposed for the differential effect of the variant on glutamatergic neurons, NFS and FS GABAergic neurons may express different KCNT1 isoforms and/or interacting channels and proteins that alter the functional effects of the variant. Alternatively, FS neurons already show a large K^+ conductance at subthreshold voltages. This is reflected in their low R_{in}, fast time constant, and high rheobase and caused by high expression of K^+ leak channels (Okaty et al., 2009). The relatively small effect of KCNT1 GOF on FS neurons may simply reflect the fact that adding a KCNT1-mediated K^+ conductance on top of an already large K^+ conductance may have little effect.

KCNT1 and other K^+ channel GOF epilepsies are typically treatment resistant, and the use of quinidine, which inhibits most *KCNT1* GOF variant currents in heterologous neurons, has shown limited success in treating KCNT1-related epilepsy in humans. Here, we show that *Kcnt1*$^{m/m}$ neurons, networks, and mice all display clear pathology at 2 weeks of age. In addition to the changes in membrane excitability, which may be correctable by blocking KCNT1 or other ion channel currents, we also found increases in C_m and synaptic P_c at multiple synaptic motifs, which likely play a role in the generation of abnormal network activity. These structural changes would be more difficult to reverse by modulating ion channel currents, unless perhaps the modulation occurred prior to their occurrence, which would argue for earlier treatment with quinidine (Dilena et al., 2018). Alternatively, if the Na_P current activates the increased K_{Na} current and results in reduced interneuron excitability, drugs that inhibit the Na_P current could have the dually useful effect of mitigating aberrant activation of the K_{Na} current in NFS GABAergic neurons while still providing general dampening of membrane excitability in glutamatergic neurons. Na_P current inhibitors are currently available and have been used with success in preclinical models of Na^+ channel dysfunction (Baker et al., 2018; Anderson et al., 2014). Our data suggest that the way forward to designing optimal treatment strategies for genetic epilepsies is a better understanding of the complex interactions among neuron-subtype-specific membrane currents, circuit development, and synaptic connections.

STAR★METHODS

Detailed methods are provided in the online version of this paper and include the following:

- KEY RESOURCES TABLE
- RESOURCE AVAILABILITY
  - Lead Contact
  - Materials Availability
  - Data and Code Availability
- EXPERIMENTAL MODEL AND SUBJECT DETAILS
  - Mice
  - Primary Astrocyte Feeder Layer Culture
  - Primary Cortical Neuron Culture for Electrophysiology
- METHOD DETAILS
  - Western Blotting
  - Mouse Brain Morphology and Histology
  - Mouse Behavioral Tasks – Open Field Exploration
  - Mouse Behavioral Tasks – Elevated Plus Maze
  - Mouse Behavioral Tasks – Acoustic Startle Response
  - Mouse Behavioral Tasks – Fear Conditioning
  - Mouse Behavioral Tasks – Nesting
  - Video-Electroencephalogram
  - Widefield Calcium Imaging
  - Mouse Pup Electrocorticography
  - Cortical Neuron Culture Electrophysiology
  - K_{Na} Current Measurements
  - Multi-electrode Arrays
  - Slice Electrophysiology
- QUANTIFICATION AND STATISTICAL ANALYSIS

SUPPLEMENTAL INFORMATION

Supplemental Information can be found online at https://doi.org/10.1016/j.celrep.2020.108303.

ACKNOWLEDGMENTS

This work was supported by NIH/NINDS grants NS087095 (M.C.W.), NS110945 (M.C.W.), NS031348 (W.N.F.), and OD020351 (The Jackson Laboratory Center for Precision Genetics). This project also received funding from the European Union's Horizon 2020 research and innovation programme

under the Marie Skłodowska-Curie grant agreement No 799501 (S.D.). The authors would like to acknowledge the support of the Microscopy Imaging Center and the Cellular & Molecular Core at the University of Vermont, especially Dr. Todd Clason, and Dr. Rod Scott for advice on statistical modeling.

AUTHOR CONTRIBUTIONS

Conceptualization, D.B.G., M.J.B., W.N.F., and M.C.W.; Methodology, D.W., D.K., M.Y., and C.M.L.; Formal Analysis, A.N.S., S.C., E.R.C, W.F.T., Y.P., J.N.G., and M.C.W.; Investigation, A.N.S., S.C., S.P., E.R.C., W.F.T., S.D., C.D.B., M.A.B., and M.C.W.; Writing – Original Draft, A.N.S., S.C., W.F.T., J.N.G., W.N.F., and M.C.W.; Writing – Review & Editing, A.N.S., S.C., M.J.B., W.N.F., and M.C.W.; Supervision, M.Y., J.N.G, D.B.G., M.J.B., W.N.F., and M.C.W.; Funding Acquisition, D.B.G., W.N.F., and M.C.W.

DECLARATION OF INTERESTS

S.C. serves a consultant for Q-State Biosciences. D.B.G. is a founder of and holds equity in Praxis, serves as a consultant to AstraZeneca, and has received research support from Janssen, Gilead, Biogen, AstraZeneca, and UCB. M.J.B. has received research support from Janssen. The remaining authors declare no competing interests.

Received: December 4, 2019
Revised: August 6, 2020
Accepted: October 1, 2020
Published: October 27, 2020

REFERENCES

Anderson, L.L., Thompson, C.H., Hawkins, N.A., Nath, R.D., Petersohn, A.A., Rajamani, S., Bush, W.S., Frankel, W.N., Vanoye, C.G., Kearney, J.A., and George, A.L., Jr. (2014). Antiepileptic activity of preferential inhibitors of persistent sodium current. Epilepsia *55*, 1274–1283.

Asinof, S., Mahaffey, C., Beyer, B., Frankel, W.N., and Boumil, R. (2016). Dynamin 1 isoform roles in a mouse model of severe childhood epileptic encephalopathy. Neurobiol. Dis. *95*, 1–11.

Avermann, M., Tomm, C., Mateo, C., Gerstner, W., and Petersen, C.C. (2012). Microcircuits of excitatory and inhibitory neurons in layer 2/3 of mouse barrel cortex. J. Neurophysiol. *107*, 3116–3134.

Baker, E.M., Thompson, C.H., Hawkins, N.A., Wagnon, J.L., Wengert, E.R., Patel, M.K., George, A.L., Jr., Meisler, M.H., and Kearney, J.A. (2018). The novel sodium channel modulator GS-458967 (GS967) is an effective treatment in a mouse model of SCN8A encephalopathy. Epilepsia *59*, 1166–1176.

Barcia, G., Fleming, M.R., Deligniere, A., Gazula, V.R., Brown, M.R., Langouet, M., Chen, H., Kronengold, J., Abhyankar, A., Cilio, R., et al. (2012). De novo gain-of-function KCNT1 channel mutations cause malignant migrating partial seizures of infancy. Nat. Genet. *44*, 1255–1259.

Barrows, C.M., McCabe, M.P., Chen, H., Swann, J.W., and Weston, M.C. (2017). PTEN loss increases the connectivity of fast synaptic motifs and functional connectivity in a developing hippocampal network. J. Neurosci. *37*, 8595–8611.

Bearden, D., Strong, A., Ehnot, J., DiGiovine, M., Dlugos, D., and Goldberg, E.M. (2014). Targeted treatment of migrating partial seizures of infancy with quinidine. Ann. Neurol. *76*, 457–461.

Bhattacharjee, A., Gan, L., and Kaczmarek, L.K. (2002). Localization of the Slack potassium channel in the rat central nervous system. J. Comp. Neurol. *454*, 241–254.

Bhattacharjee, A., von Hehn, C.A., Mei, X., and Kaczmarek, L.K. (2005). Localization of the Na+-activated K+ channel Slick in the rat central nervous system. J. Comp. Neurol. *484*, 80–92.

Budelli, G., Hage, T.A., Wei, A., Rojas, P., Jong, Y.J., O'Malley, K., and Salkoff, L. (2009). Na+-activated K+ channels express a large delayed outward current in neurons during normal physiology. Nat. Neurosci. *12*, 745–750.

Casale, A.E., Foust, A.J., Bal, T., and McCormick, D.A. (2015). Cortical interneuron subtypes vary in their axonal action potential properties. J. Neurosci. *35*, 15555–15567.

Cervantes, B., Vega, R., Limón, A., and Soto, E. (2013). Identity, expression and functional role of the sodium-activated potassium current in vestibular ganglion afferent neurons. Neuroscience *240*, 163–175.

Chen, H., Kronengold, J., Yan, Y., Gazula, V.R., Brown, M.R., Ma, L., Ferreira, G., Yang, Y., Bhattacharjee, A., Sigworth, F.J., et al. (2009). The N-terminal domain of Slack determines the formation and trafficking of Slick/Slack heteromeric sodium-activated potassium channels. J. Neurosci. *29*, 5654–5665.

Chong, P.F., Nakamura, R., Saitsu, H., Matsumoto, N., and Kira, R. (2016). Ineffective quinidine therapy in early onset epileptic encephalopathy with KCNT1 mutation. Ann. Neurol. *79*, 502–503.

De Stasi, A.M., Farisello, P., Marcon, I., Cavallari, S., Forli, A., Vecchia, D., Losi, G., Mantegazza, M., Panzeri, S., Carmignoto, G., et al. (2016). Unaltered network activity and interneuronal firing during spontaneous cortical dynamics in vivo in a mouse model of severe myoclonic epilepsy of infancy. Cereb. Cortex *26*, 1778–1794.

Deacon, R.M. (2006). Assessing nest building in mice. Nat. Protoc. *1*, 1117–1119.

Dilena, R., DiFrancesco, J.C., Soldovieri, M.V., Giacobbe, A., Ambrosino, P., Mosca, I., Galli, M.A., Guez, S., Fumagalli, M., Miceli, F., et al. (2018). Early treatment with quinidine in 2 patients with epilepsy of infancy with migrating focal seizures (EIMFS) due to gain-of-function KCNT1 mutations: functional studies, clinical responses, and critical issues for personalized therapy. Neurotherapeutics *15*, 1112–1126.

Du, W., Bautista, J.F., Yang, H., Diez-Sampedro, A., You, S.A., Wang, L., Kotagal, P., Lüders, H.O., Shi, J., Cui, J., et al. (2005). Calcium-sensitive potassium channelopathy in human epilepsy and paroxysmal movement disorder. Nat. Genet. *37*, 733–738.

Farrell, J.S., Nguyen, Q.A., and Soltesz, I. (2019). Resolving the micro-macro disconnect to address core features of seizure networks. Neuron *101*, 1016–1028.

Fenoglio-Simeone, K.A., Wilke, J.C., Milligan, H.L., Allen, C.N., Rho, J.M., and Maganti, R.K. (2009). Ketogenic diet treatment abolishes seizure periodicity and improves diurnal rhythmicity in epileptic Kcna1-null mice. Epilepsia *50*, 2027–2034.

Fitzgerald, M.P., Fiannacca, M., Smith, D.M., Gertler, T.S., Gunning, B., Syrbe, S., Verbeek, N., Stamberger, H., Weckhuysen, S., Ceulemans, B., et al. (2019). Treatment responsiveness in KCNT1-related epilepsy. Neurotherapeutics *16*, 848–857.

Franceschetti, S., Lavazza, T., Curia, G., Aracri, P., Panzica, F., Sancini, G., Avanzini, G., and Magistretti, J. (2003). Na+-activated K+ current contributes to postexcitatory hyperpolarization in neocortical intrinsically bursting neurons. J. Neurophysiol. *89*, 2101–2111.

Gelfman, S., Wang, Q., Lu, Y.F., Hall, D., Bostick, C.D., Dhindsa, R., Halvorsen, M., McSweeney, K.M., Cotterill, E., Edinburgh, T., et al. (2018). meaRtools: An R package for the analysis of neuronal networks recorded on microelectrode arrays. PLoS Comput. Biol. *14*, e1006506.

Gelinas, J.N., Khodagholy, D., Thesen, T., Devinsky, O., and Buzsáki, G. (2016). Interictal epileptiform discharges induce hippocampal-cortical coupling in temporal lobe epilepsy. Nat. Med. *22*, 641–648.

Gertler, T., Bearden, D., Bhattacharjee, A., and Carvill, G. (2018). KCNT1-related epilepsy. In GeneReviews, M.P. Adam, H.H. Ardinger, R.A. Pagon, S.E. Wallace, L.J.H. Bean, K. Stephens, and A. Amemiya, eds. (University of Washington).

Glasscock, E., Yoo, J.W., Chen, T.T., Klassen, T.L., and Noebels, J.L. (2010). Kv1.1 potassium channel deficiency reveals brain-driven cardiac dysfunction as a candidate mechanism for sudden unexplained death in epilepsy. J. Neurosci. *30*, 5167–5175.

Hage, T.A., and Salkoff, L. (2012). Sodium-activated potassium channels are functionally coupled to persistent sodium currents. J. Neurosci. *32*, 2714–2721.

Heron, S.E., Smith, K.R., Bahlo, M., Nobili, L., Kahana, E., Licchetta, L., Oliver, K.L., Mazarib, A., Afawi, Z., Korczyn, A., et al. (2012). Missense mutations in the sodium-gated potassium channel gene KCNT1 cause severe autosomal dominant nocturnal frontal lobe epilepsy. Nat. Genet. *44*, 1188–1190.

Jirkof, P. (2014). Burrowing and nest building behavior as indicators of well-being in mice. J. Neurosci. Methods *234*, 139–146.

Joiner, W.J., Tang, M.D., Wang, L.Y., Dworetzky, S.I., Boissard, C.G., Gan, L., Gribkoff, V.K., and Kaczmarek, L.K. (1998). Formation of intermediate-conductance calcium-activated potassium channels by interaction of Slack and Slo subunits. Nat. Neurosci. *1*, 462–469.

Kim, G.E., and Kaczmarek, L.K. (2014). Emerging role of the KCNT1 Slack channel in intellectual disability. Front. Cell. Neurosci. *8*, 209.

Kim, U., and McCormick, D.A. (1998). Functional and ionic properties of a slow afterhyperpolarization in ferret perigeniculate neurons in vitro. J. Neurophysiol. *80*, 1222–1235.

Kim, G.E., Kronengold, J., Barcia, G., Quraishi, I.H., Martin, H.C., Blair, E., Taylor, J.C., Dulac, O., Colleaux, L., Nabbout, R., and Kaczmarek, L.K. (2014). Human Slack potassium channel mutations increase positive cooperativity between individual channels. Cell Rep. *9*, 1661–1672.

Kim, T.H., Zhang, Y., Lecoq, J., Jung, J.C., Li, J., Zeng, H., Niell, C.M., and Schnitzer, M.J. (2016). Long-term optical access to an estimated one million neurons in the live mouse cortex. Cell Rep. *17*, 3385–3394.

Klaassen, A., Glykys, J., Maguire, J., Labarca, C., Mody, I., and Boulter, J. (2006). Seizures and enhanced cortical GABAergic inhibition in two mouse models of human autosomal dominant nocturnal frontal lobe epilepsy. Proc. Natl. Acad. Sci. USA *103*, 19152–19157.

Köhling, R., and Wolfart, J. (2016). Potassium channels in epilepsy. Cold Spring Harb. Perspect. Med. *6*, 6.

Lee, S., Hjerling-Leffler, J., Zagha, E., Fishell, G., and Rudy, B. (2010). The largest group of superficial neocortical GABAergic interneurons expresses ionotropic serotonin receptors. J. Neurosci. *30*, 16796–16808.

Lee, H., Lin, M.C., Kornblum, H.I., Papazian, D.M., and Nelson, S.F. (2014). Exome sequencing identifies de novo gain of function missense mutation in KCND2 in identical twins with autism and seizures that slows potassium channel inactivation. Hum. Mol. Genet. *23*, 3481–3489.

Liu, X., and Stan Leung, L. (2004). Sodium-activated potassium conductance participates in the depolarizing afterpotential following a single action potential in rat hippocampal CA1 pyramidal cells. Brain Res. *1023*, 185–192.

Lozovaya, N., Gataullina, S., Tsintsadze, T., Tsintsadze, V., Pallesi-Pocachard, E., Minlebaev, M., Goriounova, N.A., Buhler, E., Watrin, F., Shityakov, S., et al. (2014). Selective suppression of excessive GluN2C expression rescues early epilepsy in a tuberous sclerosis murine model. Nat. Commun. *5*, 4563.

Lu, R., Bausch, A.E., Kallenborn-Gerhardt, W., Stoetzer, C., Debruin, N., Ruth, P., Geisslinger, G., Leffler, A., Lukowski, R., and Schmidtko, A. (2015). Slack channels expressed in sensory neurons control neuropathic pain in mice. J. Neurosci. *35*, 1125–1135.

Mack, C.M., Lin, B.J., Turner, J.D., Johnstone, A.F., Burgoon, L.D., and Shafer, T.J. (2014). Burst and principal components analyses of MEA data for 16 chemicals describe at least three effects classes. Neurotoxicology *40*, 75–85.

Madisen, L., Garner, A.R., Shimaoka, D., Chuong, A.S., Klapoetke, N.C., Li, L., van der Bourg, A., Niino, Y., Egolf, L., Monetti, C., et al. (2015). Transgenic mice for intersectional targeting of neural sensors and effectors with high specificity and performance. Neuron *85*, 942–958.

Markram, H., Muller, E., Ramaswamy, S., Reimann, M.W., Abdellah, M., Sanchez, C.A., Ailamaki, A., Alonso-Nanclares, L., Antille, N., Arsever, S., et al. (2015). Reconstruction and simulation of neocortical microcircuitry. Cell *163*, 456–492.

Martinez-Espinosa, P.L., Wu, J., Yang, C., Gonzalez-Perez, V., Zhou, H., Liang, H., Xia, X.M., and Lingle, C.J. (2015). Knockout of Slo2.2 enhances itch, abolishes KNa current, and increases action potential firing frequency in DRG neurons. eLife *4*, 4.

McConnell, E.R., McClain, M.A., Ross, J., Lefew, W.R., and Shafer, T.J. (2012). Evaluation of multi-well microelectrode arrays for neurotoxicity screening using a chemical training set. Neurotoxicology *33*, 1048–1057.

McTague, A., Nair, U., Malhotra, S., Meyer, E., Trump, N., Gazina, E.V., Papandreou, A., Ngoh, A., Ackermann, S., Ambegaonkar, G., et al. (2018). Clinical and molecular characterization of *KCNT1*-related severe early-onset epilepsy. Neurology *90*, e55–e66.

Miceli, F., Soldovieri, M.V., Ambrosino, P., De Maria, M., Migliore, M., Migliore, R., and Taglialatela, M. (2015). Early-onset epileptic encephalopathy caused by gain-of-function mutations in the voltage sensor of Kv7.2 and Kv7.3 potassium channel subunits. J. Neurosci. *35*, 3782–3793.

Mikati, M.A., Jiang, Y.H., Carboni, M., Shashi, V., Petrovski, S., Spillmann, R., Milligan, C.J., Li, M., Grefe, A., McConkie, A., et al. (2015). Quinidine in the treatment of KCNT1-positive epilepsies. Ann. Neurol. *78*, 995–999.

Millichap, J.J., Miceli, F., De Maria, M., Keator, C., Joshi, N., Tran, B., Soldovieri, M.V., Ambrosino, P., Shashi, V., Mikati, M.A., et al. (2017). Infantile spasms and encephalopathy without preceding neonatal seizures caused by KCNQ2 R198Q, a gain-of-function variant. Epilepsia *58*, e10–e15.

Milligan, C.J., Li, M., Gazina, E.V., Heron, S.E., Nair, U., Trager, C., Reid, C.A., Venkat, A., Younkin, D.P., Dlugos, D.J., et al. (2014). KCNT1 gain of function in 2 epilepsy phenotypes is reversed by quinidine. Ann. Neurol. *75*, 581–590.

Møller, R.S., Heron, S.E., Larsen, L.H., Lim, C.X., Ricos, M.G., Bayly, M.A., van Kempen, M.J., Klinkenberg, S., Andrews, I., Kelley, K., et al. (2015). Mutations in KCNT1 cause a spectrum of focal epilepsies. Epilepsia *56*, e114–e120.

Mullen, S.A., Carney, P.W., Roten, A., Ching, M., Lightfoot, P.A., Churilov, L., Nair, U., Li, M., Berkovic, S.F., Petrou, S., and Scheffer, I.E. (2018). Precision therapy for epilepsy due to *KCNT1* mutations: A randomized trial of oral quinidine. Neurology *90*, e67–e72.

Musall, S., Kaufman, M.T., Juavinett, A.L., Gluf, S., and Churchland, A.K. (2019). Single-trial neural dynamics are dominated by richly varied movements. Nat. Neurosci. *22*, 1677–1686.

Niday, Z., and Tzingounis, A.V. (2018). Potassium channel gain of function in epilepsy: an unresolved paradox. Neuroscientist *24*, 368–380.

Noebels, J. (2017). Precision physiology and rescue of brain ion channel disorders. J. Gen. Physiol. *149*, 533–546.

Ohba, C., Kato, M., Takahashi, N., Osaka, H., Shiihara, T., Tohyama, J., Nabatame, S., Azuma, J., Fujii, Y., Hara, M., et al. (2015). De novo KCNT1 mutations in early-onset epileptic encephalopathy. Epilepsia *56*, e121–e128.

Okaty, B.W., Miller, M.N., Sugino, K., Hempel, C.M., and Nelson, S.B. (2009). Transcriptional and electrophysiological maturation of neocortical fast-spiking GABAergic interneurons. J. Neurosci. *29*, 7040–7052.

Oyrer, J., Maljevic, S., Scheffer, I.E., Berkovic, S.F., Petrou, S., and Reid, C.A. (2018). Ion channels in genetic epilepsy: from genes and mechanisms to disease-targeted therapies. Pharmacol. Rev. *70*, 142–173.

Phillips, H.A., Scheffer, I.E., Berkovic, S.F., Hollway, G.E., Sutherland, G.R., and Mulley, J.C. (1995). Localization of a gene for autosomal dominant nocturnal frontal lobe epilepsy to chromosome 20q 13.2. Nat. Genet. *10*, 117–118.

Quraishi, I.H., Stern, S., Mangan, K.P., Zhang, Y., Ali, S.R., Mercier, M.R., Marchetto, M.C., McLachlan, M.J., Jones, E.M., Gage, F.H., and Kaczmarek, L.K. (2019). An epilepsy-associated KCNT1 mutation enhances excitability of human iPSC-derived neurons by increasing Slack K_{Na} currents. J. Neurosci. *39*, 7438–7449.

Quraishi, I.H., Mercier, M.R., McClure, H., Couture, R.L., Schwartz, M.L., Lukowski, R., Ruth, P., and Kaczmarek, L.K. (2020). Impaired motor skill learning and altered seizure susceptibility in mice with loss or gain of function of the Kcnt1 gene encoding Slack ($K_{Na}1.1$) Na^+-activated K^+ channels. Sci. Rep. *10*, 3213.

Reijntjes, D.O.J., Lee, J.H., Park, S., Schubert, N.M.A., van Tuinen, M., Vijayakumar, S., Jones, T.A., Jones, S.M., Gratton, M.A., Xia, X.M., et al. (2019). Sodium-activated potassium channels shape peripheral auditory function and activity of the primary auditory neurons in mice. Sci. Rep. *9*, 2573.

Rizzi, S., Knaus, H.G., and Schwarzer, C. (2016). Differential distribution of the sodium-activated potassium channels Slick and Slack in mouse brain. J. Comp. Neurol. *524*, 2093–2116.

Rossi, L.F., Wykes, R.C., Kullmann, D.M., and Carandini, M. (2017). Focal cortical seizures start as standing waves and propagate respecting homotopic connectivity. Nat. Commun. *8*, 217.

Roundtree, H.M., Simeone, T.A., Johnson, C., Matthews, S.A., Samson, K.K., and Simeone, K.A. (2016). Orexin receptor antagonism improves sleep and reduces seizures in Kcna1-null mice. Sleep (Basel) *39*, 357–368.

Rubinstein, M., Han, S., Tai, C., Westenbroek, R.E., Hunker, A., Scheuer, T., and Catterall, W.A. (2015). Dissecting the phenotypes of Dravet syndrome by gene deletion. Brain *138*, 2219–2233.

Schwindt, P.C., Spain, W.J., and Crill, W.E. (1989). Long-lasting reduction of excitability by a sodium-dependent potassium current in cat neocortical neurons. J. Neurophysiol. *61*, 233–244.

Simons, C., Rash, L.D., Crawford, J., Ma, L., Cristofori-Armstrong, B., Miller, D., Ru, K., Baillie, G.J., Alanay, Y., Jacquinet, A., et al. (2015). Mutations in the voltage-gated potassium channel gene KCNH1 cause Temple-Baraitser syndrome and epilepsy. Nat. Genet. *47*, 73–77.

Singh, N.A., Otto, J.F., Dahle, E.J., Pappas, C., Leslie, J.D., Vilaythong, A., Noebels, J.L., White, H.S., Wilcox, K.S., and Leppert, M.F. (2008). Mouse models of human KCNQ2 and KCNQ3 mutations for benign familial neonatal convulsions show seizures and neuronal plasticity without synaptic reorganization. J. Physiol. *586*, 3405–3423.

Smart, S.L., Lopantsev, V., Zhang, C.L., Robbins, C.A., Wang, H., Chiu, S.Y., Schwartzkroin, P.A., Messing, A., and Tempel, B.L. (1998). Deletion of the K(V) 1.1 potassium channel causes epilepsy in mice. Neuron *20*, 809–819.

Steinmetz, N.A., Buetfering, C., Lecoq, J., Lee, C.R., Peters, A.J., Jacobs, E.A.K., Coen, P., Ollerenshaw, D.R., Valley, M.T., de Vries, S.E.J., et al. (2017). Aberrant cortical activity in multiple GCaMP6-expressing transgenic mouse lines. eNeuro *4*, 4.

Sutor, B., and Zolles, G. (2001). Neuronal nicotinic acetylcholine receptors and autosomal dominant nocturnal frontal lobe epilepsy: a critical review. Pflugers Arch. *442*, 642–651.

Syrbe, S., Hedrich, U.B.S., Riesch, E., Djémié, T., Müller, S., Møller, R.S., Maher, B., Hernandez-Hernandez, L., Synofzik, M., Caglayan, H.S., et al.; EuroEPINOMICS RES consortium (2015). De novo loss- or gain-of-function mutations in KCNA2 cause epileptic encephalopathy. Nat. Genet. *47*, 393–399.

Tang, Q.Y., Zhang, F.F., Xu, J., Wang, R., Chen, J., Logothetis, D.E., and Zhang, Z. (2016). Epilepsy-related Slack channel mutants lead to channel over-activity by two different mechanisms. Cell Rep. *14*, 129–139.

Tran, C.H., Vaiana, M., Nakuci, J., Somarowthu, A., Goff, K.M., Goldstein, N., Murthy, P., Muldoon, S.F., and Goldberg, E.M. (2020). Interneuron desynchronization precedes seizures in a mouse model of Dravet syndrome. J. Neurosci. *40*, 2764–2775.

Tremblay, R., Lee, S., and Rudy, B. (2016). GABAergic interneurons in the neocortex: from cellular properties to circuits. Neuron *91*, 260–292.

Villa, C., and Combi, R. (2016). Potassium channels and human epileptic phenotypes: an updated overview. Front. Cell. Neurosci. *10*, 81.

Wallén, P., Robertson, B., Cangiano, L., Löw, P., Bhattacharjee, A., Kaczmarek, L.K., and Grillner, S. (2007). Sodium-dependent potassium channels of a Slack-like subtype contribute to the slow afterhyperpolarization in lamprey spinal neurons. J. Physiol. *585*, 75–90.

Wang, Quanxin (2020). Cell. https://doi.org/10.1016/j.cell.2020.04.007.

Wekselblatt, J.B., Flister, E.D., Piscopo, D.M., and Niell, C.M. (2016). Large-scale imaging of cortical dynamics during sensory perception and behavior. J. Neurophysiol. *115*, 2852–2866.

Yang, B., Desai, R., and Kaczmarek, L.K. (2007). Slack and Slick K(Na) channels regulate the accuracy of timing of auditory neurons. J. Neurosci. *27*, 2617–2627.

Yang, M., Bozdagi, O., Scattoni, M.L., Wöhr, M., Roullet, F.I., Katz, A.M., Abrams, D.N., Kalikhman, D., Simon, H., Woldeyohannes, L., et al. (2012). Reduced excitatory neurotransmission and mild autism-relevant phenotypes in adolescent Shank3 null mutant mice. J. Neurosci. *32*, 6525–6541.

Yang, Y., Vasylyev, D.V., Dib-Hajj, F., Veeramah, K.R., Hammer, M.F., Dib-Hajj, S.D., and Waxman, S.G. (2013). Multistate structural modeling and voltage-clamp analysis of epilepsy/autism mutation Kv10.2-R327H demonstrate the role of this residue in stabilizing the channel closed state. J. Neurosci. *33*, 16586–16593.

STAR★METHODS

KEY RESOURCES TABLE

REAGENT or RESOURCE	SOURCE	IDENTIFIER
Antibodies		
mouse monoclonal anti-KCNT1 (S3-26)	Abcam	Cat# ab94578; RRID:AB_10674494
goat anti-mouse IgG polyclonal, HRP-conjugated	Santa Cruz Biotechnology	Cat# sc-2005; RRID:AB_631736
mouse monoclonal anti-β-Actin (C4)	Santa Cruz Biotechnology	Cat# sc-47778 HRP; RRID:AB_2714189
Bacterial and Virus Strains		
AAV-*CaMKIIa*-GFP, serotype 8	UNC Gene Therapy Center – Vector Core	N/A
Chemicals, Peptides, and Recombinant Proteins		
NlaIII	NEB	Cat# R0125S
0.5% Trypsin-EDTA	GIBCO	Cat# 25300-054
DMEM media supplemented with Glutamine	GIBCO	Cat# 10569-010
Fetal bovine serum	GE Healthcare	Cat# SH3008803
MITO+ Serum Extender	Corning	Cat# 355006
Penicillin/Streptomycin	GIBCO	Cat# 15140-122
Collagen I	Corning	Cat# 354236
Poly-D-lysine	Sigma-Aldrich	Cat# P6407
Papain	Worthington Biochemical	Cat# LS003126
Trypsin inhibitor, Ovomucoid	Worthington Biochemical	Cat# LS003085
Neurobasal-A medium	GIBCO	Cat# 10888-022
GlutaMAX	GIBCO	Cat# 35050-061
B27 supplement	GIBCO	Cat# 17504-044
Tribromoethanol	Sigma-Aldrich	Cat# T48402
NBQX disodium salt	Tocris	Cat# 1044
Bicuculine Methiodide	Hello Bio	Cat# HB0893
Tetrodotoxin Citrate	Abcam	Cat# ab120055
Poly-D-lysine	Sigma-Aldrich	Cat# P0899-50MG
Hibernate A solution	GIBCO	Cat# A1247501
Papain-for MEA protocol	Worthington Biochemical	Cat# LK003178
DNase I	Worthington Biochemical	Cat# LK003172
HEPES	GIBCO	Cat# 15630-080
Fetal bovine serum-for MEA protocol	GIBCO	Cat# 26140-079
Laminin	Sigma-Aldrich	Cat# L2020
Critical Commercial Assays		
My Taq	Bioline	Cat# BIO-25041
Pierce BCA Protein Assay Kit	Thermo Fisher Scientific	Cat# 23225
NeuroGrid	Intan Technologies	Cat# RHD2000
Classic MEA 48	Axion Biosystems	Cat# M768-KAP-48
Experimental Models: Cell Lines		
Primary astrocyte feeder layer	This paper	N/A
Primary cortical neurons	This paper	N/A
Experimental Models: Organisms/Strains		
Mouse: Kcnt1$^{em1(Y777H)Frk}$	This paper	N/A
Mouse: C57BL/6NJ	The Jackson Laboratory	Cat# JAX:005304; RRID:IMSR_JAX:005304
Mouse: FVB.129P2-Pde6b^{+} Tyr$^{c\text{-}ch}$/AntJ	The Jackson Laboratory	Cat# JAX:004828; RRID:IMSR_JAX:004828

(*Continued on next page*)

Continued

REAGENT or RESOURCE	SOURCE	IDENTIFIER
Mouse: B6.Cg-Snap25$^{tm3.1Hze}$/J	The Jackson Laboratory	Cat# JAX:025111; RRID:IMSR_JAX:025111
Mouse: C57BL/6J	The Jackson Laboratory	Cat# JAX:000664; RRID:IMSR_JAX:000664
Oligonucleotides		
Primer: *Kcnt1* Forward: 5′-CTAGGGCTGCAAACACAACA-3′	This paper	N/A
Primer: *Kcnt1* Reverse: 5′-TCAAGCAGCAACACGATAGG-3′	This paper	N/A
Software and Algorithms		
NIS Elements Software	Nikon Instruments	RRID:SCR_014329
Med-PC V Software Suite, 64-bit	Med Associates	Cat# SOF-736
SR-LAB Startle Response System Software	San Diego Instruments	N/A
Video Freeze Software	Med Associates	Cat# SOF-843; RRID:SCR_014574
Profusion EEG 5 Software	Compumedics	N/A
SVD code	University College London – Cortex Lab	https://github.com/cortex-lab/widefield
MATLAB	MathWorks	RRID:SCR_001622
pCLAMP Clampex Software (10.3 or 10.5)	Molecular Devices	RRID:SCR_011323
Axograph X Software	Axograph Scientific	RRID:SCR_014284
AxIS Software v2.4	Axion Biosystems	RRID:SCR_016308
R package - meaRtools	Gelfman et al., 2018	https://cran.r-project.org/web/packages/meaRtools/
NeuroExplorer Software	Nex Technologies	RRID:SCR_001818
Prism 7	GraphPad	RRID:SCR_002798
SPSS	IBM	RRID:SCR_002865

RESOURCE AVAILABILITY

Lead Contact

Further information and requests for resources and reagents should be directed to and will be fulfilled by the Lead Contact, Matthew C. Weston (mcweston@uvm.edu).

Materials Availability

The *Kcnt1*^{Y777H} mouse line is available from the Lead Contact, Matthew C. Weston (mcweston@uvm.edu), with a completed Materials Transfer Agreement.

Data and Code Availability

This study did not generate datasets or code.

EXPERIMENTAL MODEL AND SUBJECT DETAILS

Mice

All mice were bred, and procedures were conducted at the Jackson Laboratory, at Columbia University Irving Medical Center, or at the University of Vermont. Each institution is fully accredited by the Association for Assessment and Accreditation of Laboratory Animal Care, and all protocols were approved by their respective Institutional Animal Care and Use Committees. All experiments were performed in accordance with respective state and federal Animal Welfare Acts and the policies of the Public Health Service. The animal protocol numbers for Columbia University were: AC-AAAU8484, AC-AAAZ8450, AC-AAAR4414, AC-AAAU8476, and AC-AAAT6474, and the University of Vermont were: 16-001 and 19-034.

Kcnt1^{Y777H} knockin mice (formal gene and allele symbol: *Kcnt1*$^{em1(Y777H)Frk}$) were generated in the C57BL/6NJ (B6NJ) mouse strain (The Jackson Laboratory, JAX: 005304) using CRISPR/Cas9 and an oligonucleotide donor sequence as part of the Jackson Laboratory Center for Precision Genetics program (JCPG, https://www.jax.org/research-and-faculty/research-centers/precision-genetics-center), and maintained by backcrossing heterozygous males to wild-type B6NJ females. *Kcnt1*^{Y777H} mice were genotyped using PCR amplification primers (*Kcnt1* forward primer: 5′-CTAGGGCTGCAAACACAACA-3′; *Kcnt1* reverse

primer: 5′-TCAAGCAGCAACACGATAGG-3′) with standard thermocycler amplification conditions using MyTaq master mix (Bioline, BIO-25041), and the annealing temperature set at 58°C. Following amplification, a restriction cut was performed with the enzyme *Nla*III (NEB, R0125S) to distinguish mutant (127 and 44 bp products after cut) from wild-type alleles (171 bp product). For some experiments, as noted in the text, male mutant mice were crossed with FVB.129P2-Pde6b+ Tyrc-ch/AntJ (The Jackson Laboratory, JAX: 004828) dams to generate cohorts of N_2 or F_2 hybrid mice.

The following additional mouse lines and strains were used for these studies: *Snap25*-2A-GCaMP6s-D knockin (B6.Cg-Snap25$^{tm3.1Hze}$/J, The Jackson Laboratory, JAX: 025111) and C57BL/6J (The Jackson Laboratory, JAX: 000664). Mice were maintained in ventilated cages at controlled temperature (22–23°C), humidity ~60%, and 12-h light: 12-h dark cycles (lights on at 7:00 AM, off 7:00 PM). Mice had access to regular chow and water, *ad libitum*. For all experiments, male and female littermates were used for each genotype. The ages of the mice for each experiment are indicated in the Method Details section.

Primary Astrocyte Feeder Layer Culture

Astrocyte feeder layers, to support the growth and maintenance of primary neurons, were generated as previously described (Barrows et al., 2017). Briefly, cortices were dissected from P0-1 WT C57BL/6J mice of either sex. The cortices were incubated in 0.05% trypsin-EDTA (GIBCO, 25300-054) for 15 min at 37°C in a Thermomixer (Eppendorf) with gentle agitation (800 rpm). Then, the cortices were mechanically dissociated with a 1-mL pipette tip, and the cells were plated into T-75 flasks containing filter-sterilized astrocyte media [DMEM media supplemented with glutamine (GIBCO, 10569-010), 10% fetal bovine serum (FBS, GE Healthcare, SH3008803), 1X MITO+ Serum Extender (Corning, 355006), and 0.2X penicillin/streptomycin (GIBCO, 15140-122)]. After the astrocytes reached confluency, they were washed with PBS and incubated for 5 min in 0.05% trypsin-EDTA at 37°C, washed, and then resuspended in astrocyte media. Astrocytes were added to 6-well plates containing 25-mm coverslips (Carolina Biological, 633037) precoated with coating mixture [0.7 mg/ml collagen I (Corning, 354236) and 0.1 mg/ml poly-D-lysine (Sigma-Aldrich, P6407) in 10 mM acetic acid].

Primary Cortical Neuron Culture for Electrophysiology

For the primary neuron culture, the dorsomedial cortices from P0-1 WT and *Kcnt1*$^{m/m}$ mice of either sex were dissected in cold HBSS. The tissue was then digested with papain (Worthington Biochemical, LS003126) for 60-75 min and treated with an ovomucoid inhibitor solution (Worthington Biochemical, LS003085) for 10 min, both while shaking at 800 rpm at 37°C in a Thermomixer (Eppendorf). The cells were then mechanically dissociated and counted. The dissociated cells were added at 200,000 cells/well to 6-well plates containing astrocyte-coated coverslips in filter-sterilized NBA plus [Neurobasal-A medium (GIBCO, 10888-022) supplemented with 1X GlutaMAX (GIBCO, 35050-061), 1X B27 supplement (GIBCO, 17504-044), and 0.2X penicillin/streptomycin (GIBCO, 15140-122)]. After plating (12-24 h), approximately 4×10^{10} genome copies (GC) of AAV8-*CaMKIIa*-GFP, serotype 8 (UNC Gene Therapy Center - Vector Core) was added to each well to fluorescently label glutamatergic neurons. Every 3-4 days, 20%–40% of the media was replaced with fresh NBA plus.

METHOD DETAILS

Western Blotting

For crude membrane/cytosol fractioning, P0 cortices of either sex were homogenized in the following homogenization buffer: 0.32 M sucrose, 10 mM HEPES pH 7.4, 2 mM EDTA in H_2O, containing a protease, and a phosphatase, inhibitor cocktail. The samples were homogenized with a motor-driven homogenizer and centrifuged at 1000 × g for 15 min at 4°C to remove the pelleted nuclear fraction. The supernatant was further centrifuged at 16000 rpm for 20 min at 4°C to yield the cytosolic fraction in the supernatant and the pelleted membrane fraction. The pellet was resuspended in homogenization buffer. Protein concentrations were determined with the Pierce BCA Protein Assay Kit (Thermo Fisher Scientific, 23225) using BSA as a standard. Sample protein (10 μg) was mixed with 4X LDS Sample Buffer (NuPAGE, NP0007), and 10X Sample Reducing Agent (NuPAGE, NP0009), heated for 10 min at 70°C, separated on a 4%–12% Bis-Tris Mini Gel (NuPAGE, NP0321), and transferred to a PVDF membrane (Millipore, ISEQ00010). Nonspecific binding was blocked for 1 h at RT with 5% BLOTTO (Bio-Rad, 1706404) in Tris-buffered saline with 0.1% Tween (TBST). Membranes were incubated overnight at 4°C with the primary antibody mouse anti-KCNT1 (1:1000, Abcam, ab94578), washed 3 × 10 min with TBST, incubated with the secondary antibody HRP-conjugated goat anti-mouse (1:10000, Santa Cruz Biotechnology, sc-2005) in 5% BLOTTO for 1 h at RT, and washed again 3 × 10 min with TBST. Blots were incubated for 5 min with Pierce ECL Western Blotting Substrate (Thermo Fisher Scientific, 32106) and developed with a Kodak X-OMAT 2000A Processor. Blots were stripped for 15 min at RT in ReBlot Plus Strong Solution (Millipore. 2504), blocked for 30 min in 5% BLOTTO, incubated for 1 h at RT with an HRP-conjugated mouse anti-β-actin antibody (1:5000, Santa Cruz Biotechnology, sc-47778) in 5% BLOTTO, and developed as previously described. β-actin was used as a loading control.

Mouse Brain Morphology and Histology

WT, *Kcnt1*$^{m/+}$, and *Kcnt1*$^{m/m}$ littermate mice of either sex were anesthetized with 1.5%–2.5% isoflurane and oxygen at P28, or 10-12 weeks of age, and transcardially perfused with PBS, followed by 4% paraformaldehyde in PBS (pH 7.4). Brains were dissected and then post-fixed overnight in 4% paraformaldehyde at 4°C. Next, brains from 10-12-week-old mice were washed with PBS, weighed, and imaged to assess gross morphology. Then, all brains were cryoprotected with 30% sucrose until sectioning. To sec-

tion, brains were frozen in Tissue-Plus O.C.T. Compound (Fisher, 23-730-571) and sectioned into 40-μm coronal slices using a cryostat. Brain sections were stored in a cryoprotectant solution with 30% ethylene glycol, 20% glycerol, and 50% 1X PBS until use.

Brain sections from P28 mice were stained with a NeuroTrace fluorescent Nissl stain (1:50, Molecular Probes, N-21482), according to the manufacturer's instructions, and mounted in Fluoromount-G Mounting Medium, with DAPI (Fisher, 00-4959-52). Nissl-stained, whole coronal section images were continuously captured with a motorized stage and automatically stitched using a 4X objective on a Nikon-A1R-ER confocal laser microscope with NIS Elements software (eight images, 10% overlap/section).

Mouse Behavioral Tasks – Open Field Exploration

Each mouse was gently placed in the center of a clear Plexiglas arena (7.31 × 27.31 × 20.32 cm, Med Associates, ENV-510) lit with dim light (~5 lux), and allowed to ambulate freely for 60 min. Infrared (IR) beams embedded along the X, Y, Z axes of the arena automatically tracked distance moved, horizontal movement, vertical movement, stereotypies, and time spent in center zone. At the end of the test, the mouse was returned to the home cage and the arena was cleaned with 70% ethanol followed by water drying.

Mouse Behavioral Tasks – Elevated Plus Maze

The elevated plus maze test was conducted as described previously (Yang et al., 2012). The elevated plus maze consisted of two open arms (30 × 5 cm) and two closed arms (30 × 5 x 15 cm) extending from a central area (5 × 5 cm). Photo beams embedded at arm entrances registered movements. Room illumination was approximately 5 lux. The test began by placing the subject mouse in the center, facing a closed arm. The mouse was allowed to freely explore the maze for 5 min. Time spent in the open arms and closed arms, the junction, and number of entries into the open arms and closed arms, were automatically scored by the MED-PC V 64-bit software (Med Associates, SOF-736). At the end of the test, the mouse was gently removed from the maze and returned to its home cage. The maze was cleaned with 70% ethanol and wiped dry between subjects.

Mouse Behavioral Tasks – Acoustic Startle Response

Acoustic startle response was tested using the SR-LAB Startle Response System with SR-LAB software (San Diego Instruments, San Diego, CA) as described previously (Yang et al., 2012). Test sessions began by placing the mouse in the Plexiglas holding cylinder for a 5-min acclimation period. For the next 8 min, mice were presented with each of six trial types across six discrete blocks of trials, for a total of 36 trials. The intertrial interval was 10–20 s. One trial type measured the response to no stimulus (baseline movement). The other five trial types measured startle responses to 40 ms sound bursts of 80, 90, 100, 110, or 120 dB. The six trial types were presented in pseudorandom order such that each trial type was presented once within a block of six trials. Startle amplitude was measured every 1 ms over a 65 ms period beginning at the onset of the startle stimulus. The maximum startle amplitude over this sampling period was taken as the dependent variable. A background noise level of 70 dB was maintained over the duration of the test session.

Mouse Behavioral Tasks – Fear Conditioning

Training and conditioning tests were conducted in two identical chambers (Med Associates) that were calibrated to deliver identical footshocks. Each chamber was 30 × 24 × 21 cm with a clear polycarbonate front wall, two stainless side walls, and a white opaque back wall. The bottom of the chamber consisted of a removable grid floor with a waste pan underneath. When placed in the chamber, the grid floor connected with a circuit board for delivery of scrambled electric shock. Each conditioning chamber was inside a sound-attenuating environmental chamber (Med Associates). A camera mounted on the front door of the environmental chamber recorded test sessions, which were later scored automatically using the Video Freeze software (Med Associates, SOF-843). For the training session, each chamber was illuminated with a white house light. An olfactory cue was added by dabbing a drop of imitation almond flavoring solution (1:100 dilution in water) on the metal tray beneath the grid floor. The mouse was placed in the test chamber and allowed to explore freely for 2 min. A pure tone (5 kHz, 80 dB), which serves as the conditioned stimulus (CS), was played for 30 s. During the last 2 s of the tone, a footshock (0.5 mA) was delivered as the unconditioned stimulus (US). Each mouse received three CS-US pairings, separated by 90 s intervals. After the last CS-US pairing, the mouse remained in the chamber for another 120 s, during which freezing behavior was scored by the Video Freeze software. The mouse was then returned to its home cage. Contextual conditioning was tested 24 h later in the same chamber, with the same illumination and olfactory cue present but without footshock. Each mouse was placed in the chamber for 5 min, in the absence of CS and US, during which freezing was scored, and then returned to its home cage. Cued conditioning was conducted 48 h after training. Contextual cues were altered by covering the grid floor with a smooth white plastic sheet, inserting a piece of black plastic sheet bent to form a vaulted ceiling, using near infrared light instead of white light, and dabbing vanilla instead of banana odor on the floor. The session consisted of a 3 min free exploration period followed by 3 min of the identical CS tone (5 kHz, 80 dB). Freezing was scored during both 3 min segments. The mouse was then returned to its home cage, and the chamber thoroughly cleaned of odors between sessions using 70% ethanol and water.

Mouse Behavioral Tasks – Nesting

The nesting test was performed as previously described (Deacon, 2006). Briefly, mice were placed in individual cages at 6 pm, with a piece of nestlet weighing 2.5 g. The next morning, the remaining unshredded nestlet was weighed and a nesting score between 1 (no nest) and 5 (perfect nest) was attributed depending on nest quality.

Video-Electroencephalogram

Electrode implantation of adult (> 7 weeks of age) male and female mice was performed surgically as recently described (Asinof et al., 2016). Mice were anesthetized with tribromoethanol (250 mg/kg i.p., Sigma-Aldrich, T48402). Three small burr holes were drilled in the skull (1 mm rostral to the bregma on both sides and 2 mm caudal to the bregma on the left) 2 mm lateral to the midline. One hole was drilled over the cerebellum as a reference. Using four teflon-coated silver wires soldered onto the pins of a microconnector (Mouser electronics, 575-501101), the wires were placed between the dura and the brain and a dental cap was then applied. The mice were given a post-operative analgesic of carprofen (5 mg/kg subcutaneous Rimadyl injectable) and allowed a 48-h recovery period before recordings were taken. To record EEG signals, mice were connected to commutators (Plastics One) with flexible recording cables to allow unrestricted movements within the cage. Signal (200 samples/s) was acquired on a Grael II 48 EEG amplifier (Compumedics), and the data were examined in Profusion EEG 5 software (Compumedics). Differential amplification recordings were recorded pairwise between all three electrodes, as well as referential, providing a montage of six channels for each mouse. Mouse activity was captured simultaneously by video monitoring using a Sony IPELA EP550 model camera, with an infrared light to allow recordings in the dark. We recorded continuously for 24-72 h.

For sleep analysis, we used a custom-written MATLAB program to classify wake, NREM sleep, and REM sleep, and to detect GTCS and TS events. The program first used fast Fourier transform (FFT) to calculate the power spectrum of the EEG using a 5 s sliding window, sequentially shifted by 2 s increments. Then it semi-automatedly classified into different brain states using the following criteria: NREM sleep, high power at low frequencies (1-4 Hz) and low EMG activity; REM sleep, high power at theta frequencies (6-9 Hz) and low EMG activity; GTCS and TS, high power at ''seizure'' frequencies (19-23 Hz); and wake, the remaining (or default) state. We chose the 19-23 Hz band to detect seizures based on its clear separation from normal brain oscillatory activities. The classification was followed by manual inspection to further refine the scoring. Brain states prior to each GTCS/TS event were used in Table S1.

Widefield Calcium Imaging

Male and female mice that were heterozygous for the *Snap25*-GCaMP6s construct (Madisen et al., 2015) (Jackson Labs Stock No: 025111) and either homozygous Y777H or WT at the *Kcnt1* locus were generated. To gain optical access to the dorsal cortex, the animal's scalp and the underlying periosteum were removed before coating the dorsal skull with UV cure cyanoacrylate (Loctite 4305) and attaching a custom aluminum headplate to the skull. This headplate framed the glue covered skull and allowed the animal to be secured on a 20-cm diameter Styrofoam treadwheel during imaging sessions. In one homozygous mutant mouse the dorsal skull was removed entirely and replaced with a glass window (Labmaker, Crystal Skull) following a previously described protocol (Kim et al., 2016). Imaging was performed using a custom tandem-lens epifluorescence macroscope built according to a design previously described (Wekselblatt et al., 2016). This macroscope was configured for 2.1X magnification using a Nikon Nikkor 50mm f/1.2 lens paired with a Nikon 105mm f/1.8 lens. During all sessions, images were acquired at 40 Hz with an Andor Zyla 5.5 10-tap sCMOS camera set to 4 × 4-pixel binning. Successive frames were illuminated with blue and green light, and the green reflectance images were used to estimate changes in fluorescence resulting from hemodynamic factors and correct for them in GCaMP images. For blue illumination, we used an X-Cite 120 LED (Lumen Dynamics, XT120L) with a filter set consisting of an ET470/40x excitation filter, a T495lpxr dichroic, and an ET525/50 m emission filter (Set 49002, Chroma Technology, Bellows Falls, VT). Total blue light power delivered to the implant typically ranged from 18-21 mW. For green illumination, we used a 530 nm 6.8 mW Thorlabs LED (M530F2) driven by a Thorlabs tcube (LEDD1B) coupled to a fiber optic obliquely pointed at the brain. To switch illumination sources between frames, we relied on an Arduino Uno R3 (A000066) microcontroller operating on the Zyla 'expose' signal. At the beginning of each session, we exposed a dark frame in which no illumination was used. This frame was subtracted from all illuminated frames in the session as the first processing step. Subsequently, reflectance and GCaMP images were deinterleaved and linearly interpolated from 20 to 40 Hz. We calculated $\Delta F/F$ for each pixel in the image that covered the brain, as defined by a hand-drawn mask. We estimated F for each pixel as the average of the bottom 20th percentile of fluorescent values over the entire session. Following $\Delta F/F$ calculation, we subtracted fractional green fluorescence ($\Delta F/F_{mean}$) with F_{mean} calculated over the full session. Finally, we performed Singular Value Decomposition (SVD) on the $\Delta F/F$ image stacks and reconstructed images using the first 50 singular values for all subsequent analysis. The SVD code was a modification of that provided by the Cortex Lab group at University College London. To rigidly align area borders derived from the Allen Common Coordinate Framework v3 to each brain, we relied on the landmark-based strategy previously described (Musall et al., 2019).

Mouse Pup Electrocorticography

Eight *Kcnt1*$^{m/m}$ and five WT pups of either sex at P13-15 were used for *in vivo* electrophysiology. All experiments were performed in accordance with protocols approved by IACUC at Columbia University Irving Medical Center. Pups were anesthetized using isoflurane and electromyography (EMG) electrodes were placed for real-time monitoring of respiratory rate, heart rate, and muscle activity. The animals were then given systemic and local analgesia, head-fixed, and a craniotomy was made over the dorsal cortical surface of one hemisphere. This craniotomy was centered over somatomotor cortex, spanning 2.5 mm in the mediolateral direction and 3.5 mm in the anterioposterior direction between bregma and lambda. A NeuroGrid (ultra-conformable, biocompatible surface electrocorticography array, 119 electrodes, 177 μm pitch) array was placed on the surface of the dura and covered with a piece of sterile compressed sponge. The pup was transferred to a temperature and humidity-controlled enclosure and allowed to recover for 30 min,

after which recording commenced. Signals were amplified, digitized continuously at 20 kHz using a head-stage directly attached to the NeuroGrid (RHD2000, Intan Technology), and stored for offline analysis with 16-bit format. Data were analyzed using MATLAB (MathWorks) and visualized using Neuroscope. At the completion of electrophysiological recording, pups were euthanized.

Neurophysiologic recordings were synchronized with the EMG signals to facilitate identification and elimination of any epochs with artifacts from subsequent analysis. Ictal patterns were identified using a line length algorithm and confirmed with visual screening of the raw data. Interictal epileptiform discharges were detected using previously employed frequency and duration features (Gelinas et al., 2016).

Cortical Neuron Culture Electrophysiology

Whole-cell recordings were performed with patch-clamp amplifiers (MultiClamp 700B; Molecular Devices) under the control of pClamp Clampex 10.3 or 10.5 software (Molecular Devices). Data were acquired at 20 kHz and low-pass filtered at 6 kHz. The series resistance was compensated at 70%, and only cells with series resistances maintained at less than 15 MΩ were analyzed. Patch electrodes were pulled from 1.5-mm o.d. thin-walled glass capillaries (Sutter Instruments, BF150-86-75) in five stages on a micropipette puller (model P-97; Sutter Instruments). Internal solution contained the following: 136 mM K-gluconate, 17.8 mM HEPES, 1 mM EGTA, 0.6 mM $MgCl_2$, 4 mM ATP, 0.3 mM GTP, 12 mM creatine phosphate, and 50 U/ml phosphocreatine kinase. Alternatively, internal solution contained: 136 mm KCl, 17.8 mm HEPES, 1 mm EGTA, 0.6 mm MgCl2, 4 mm ATP, 0.3 mm GTP, 12 mm creatine phosphate, and 50 U/ml phosphocreatine kinase. The pipette resistance was between 2 and 4 MΩ. Standard extracellular solution contained the following (in mM): 140 NaCl, 2.4 KCl, 10 HEPES, 10 glucose, 4 $MgCl_2$, and 2 $CaCl_2$ (pH 7.3, 305 mOsm). All experiments were performed at room temperature (22–23°C). Whole-cell recordings were performed on cortical neurons from control and mutant groups in parallel on the same day (day 13–16 *in vitro*). All experiments were performed by two independent investigators blinded to the genotypes. Electrophysiology data were analyzed offline with AxoGraph X software (AxoGraph Scientific).

For current-clamp experiments, the intrinsic electrophysiological properties of neurons were tested by injecting 500-ms square current pulses incrementing in 20 pA steps, starting at −100 pA. Resting membrane potential (V_m) was calculated from a 50 ms average before current injection. The membrane time constant (Tau, τ) was calculated from an exponential fit of current stimulus offset. Input resistance (R_{In}) was calculated from the steady state of the voltage responses to the hyperpolarizing current steps. Membrane capacitance (C_m) was calculated by dividing the time constant by the input resistance. Action potentials (APs) were evoked with 0.5 s, 20 pA depolarizing current steps. AP threshold was defined as the membrane potential at the inflection point of the rising phase of the AP. AP amplitude was defined as the difference in membrane potential between the AP peak and threshold, and the afterhyperpolarization was the difference between the AP threshold and the lowest V_m value within 50 ms. The AP half-width was defined as the width of the AP at half-maximal amplitude. The maximum depolarization and repolarization rates were determined by differentiating the AP waveform and finding the peak values. To obtain the neuron's maximum firing frequency, depolarizing currents in 20-pA steps were injected until the number of APs per stimulus reached a plateau phase. Rheobase was defined as the minimum current required to evoke an AP during the 500 ms of sustained somatic current injections. AP half-width adaptation was determined by dividing the half-width of the last AP of a train at steady state frequency by the first. AP frequency adaptation was determined by dividing the mean interspike interval of the last four APs by the minimum. The membrane potential values were not corrected for the liquid junction potential. GABAergic neurons were classified as fast spiking (FS) if their maximum mean firing rate reached above 60 Hz and their AP half-widths increased by less than 25% during the AP train (Casale et al., 2015; Avermann et al., 2012). All others were considered non-fast spiking (NFS).

For voltage-clamp experiments to measure synaptic currents, two neurons were patched simultaneously and held at −70 mV, except for evoked IPSC measurements, for which postsynaptic neurons were held at 0 mV. PSCs were triggered by a 2 ms somatic depolarization to 0 mV. The shape of the evoked response, the reversal potential and the effect of receptor antagonists [10 μM NBQX (Tocris, 1044) or 20 μM bicuculline (BIC, Hello Bio, HB0893)] were analyzed to verify the glutamatergic or GABAergic identities of the currents. Neurons were stimulated at 0.1 Hz in standard external solution to measure basal-evoked synaptic responses. Spontaneous synaptic potentials were recorded in control solution with either NBQX or bicuculline to isolate EPSCs or IPSCs, respectively. Data were filtered at 1 kHz and analyzed using template-based miniature event detection algorithms implemented in the AxoGraph X. The threshold for detection was set at three times the baseline SD from a template of 0.5 ms rise time and 3 ms decay. The E/I ratio was calculated as the product of the sEPSC frequency and charge over the sum of the sEPSC frequency and charge and the product of the sIPSC frequency and charge.

K_{Na} Current Measurements

For voltage-clamp experiments to measure the sodium-activated K^+ current, neurons were held at −70 mV and given 1 s voltage pulses in 10 mV steps over a range of −80 to +50 mV. Recordings were obtained for each cell in standard extracellular solution or extracellular solution containing 0.5 μM Tetrodotoxin (TTX, Abcam, ab120055). To minimize rundown, experiments were started only after test pulses produced stable delayed outward currents. After steps in standard solution, TTX was applied directly on the recorded neuron with a custom-built fast flow perfusion system capable of complete solution exchange in less than 1 s. After 30 −40 s in TTX, the step protocol was repeated. Current traces from the TTX solution were then subtracted from the current traces obtained from the standard solution to obtain the difference current. The difference current over the 100 ms at the end of the voltage pulse was considered the steady state K_{Na} current. Conductance (G) was calculated by dividing the current at each step by the

driving force for K^+. Activation curves were created by normalizing the G values to the maximum for each cell. The resulting curves were fit with a Boltzmann sigmoid function with the bottom constrained to 0 to obtain the voltage at half max conductance (V_{50}). Unconstrained fits excluding values at voltage steps below 0 mV to minimize the effect of the TTX-sensitive inward current showed the same significant left-shifts in FS and NFS Kcnt1$^{m/m}$ GABAergic neurons while glutamatergic neurons were not different. Slope was not significantly different for any tests.

Multi-electrode Arrays

One to seven days before isolation of cortical neurons, 48-well MEA plates (Axion Biosystems, M768-KAP-48) were coated with 50 μg/mL poly-D-lysine (Sigma-Aldrich, P0899-50MG) in borate buffer, then washed three times with PBS and stored in PBS at 4°C until use. Prior to use, PBS was aspirated, and plates were dried in a sterilized hood. Cortices were dissected from the brains of P0 C57BL/6NJ WT or *Kcnt1*$^{m/m}$ mice of either sex. Pups were decapitated, weighed, and genotyped. The entire cerebral cortex was rapidly dissected and cut into small pieces under sterile conditions in cold Hibernate A solution (GIBCO, A1247501). Cortices from two WT or *Kcnt1*$^{m/m}$ pups were pooled together. The dissected cortices were then enzymatically digested in 20 U mL^{-1} Papain plus DNase (Worthington Biochemical, LK003178 and LK003172) diluted in Hibernate A for 20 min at 37°C. Cells were pelleted by centrifugation at 300RCF for 5 min, and then the digestion was neutralized by aspirating off the supernatant and adding warm Hibernate A media. Cells were mechanically dissociated by trituration and counted using a hemocytometer with Trypan blue counterstain. Cells were pelleted by centrifugation at 300RCF for 5 min and resuspended at a density of 6,000 cells/μl in warm Neurobasal-A (GIBCO, 10888-022) + 1X B27 supplement (GIBCO, 17504-044) + 1X GlutaMax (GIBCO, 35050-061) + 1% HEPES (GIBCO, 15630-080) + 1% Penicillin/Streptomycin (GIBCO, 15140-122) + 1% FBS (GIBCO, 26140-079) + 5 ug/mL Laminin (Sigma-Aldrich, L2020). 50,000 cells were plated on a pre-coated 48-well MEA plate in a 40 μL drop. The day after plating (DIV1), 100% of the media was removed and replaced with warm Neurobasal-A + 1X B27 supplement + 1X GlutaMax + 1% HEPES + 1% Penicillin/Streptomycin (NBA/B27 medium). Glial growth was not chemically suppressed. Cultures were maintained at 37°C in 5% CO_2. Media was 50% changed every other day with fresh, warm NBA/B27 starting on DIV3, after each recording session.

MEA recordings were conducted on media change days prior to media change starting on DIV5. Plates were equilibrated for 5 min then recorded for 15 min/day using an Axion Biosystems Maestro 768 channel amplifier (Axion Biosystems) at 37°C in a CO_2 gas-controlled chamber with Axion Integrated Studios (AxIS) software v2.4 (Axion Biosystems). Each well of a 48-well plate is comprised of 16 electrodes on a 4 × 4 grid, with each electrode capturing activity of nearby neurons. A Butterworth band-pass filter (200-3000 Hz) and an adaptive threshold spike detector set at 7X the standard deviation of the noise was used during recordings. Raw data and spike list files were collected. Spike list files were used to extract additional spike, burst, and network features, using a custom MEA analysis software package for interpretation of neuronal activity patterns, meaRtools, based on rigorous permutation statistics that enables enhanced identification of over 70 activity features (Gelfman et al., 2018). Specifically, we analyzed spiking and bursting rates, burst duration, and the time between bursts (i.e., interburst interval, IBI), as well as synchronicity of the network. We determined the parameters for detecting neuronal bursts and network events based on published reports and experimentation (Mack et al., 2014; McConnell et al., 2012). Activity data were inspected to remove inactive electrodes and wells. For an electrode to be considered active, we required that at least five spikes/min were recorded. Wells in which fewer than 4 electrodes were active for > 50% of the days of recording were considered inactive and removed from analyses. For synchronous network events, at least 5 electrodes (> 25% of the total in a well) were required to participate in a network event for the network event to qualify as a network spike or burst. Events with fewer participating electrodes were filtered. Bursts were detected using the maximum interval burst detection algorithm (NeuroExplorer software, Nex Technologies) implemented in the meaRtools package. We required that a burst consist of at least 5 spikes and last at least 0.05 s, and that the maximum duration between two spikes within a burst be 0.1 s at the beginning of a burst and 0.25 s at the end of a burst. Adjacent bursts were further merged if the duration between them was less than 0.8 s. These parameters were chosen based on literature and on in-house experimentation (Mack et al., 2014). To analyze data over time, we performed permuted Mann-Whitney U tests. The values for each well for the chosen DIVs were combined and a Mann-Whitney U (MWU) test was performed. The labels for each well (WT versus *Kcnt1*$^{m/m}$) were then shuffled and permuted 1,000 times to create 1,000 datasets that were tested for significance using an MWU test. We report the permuted p values as the rank of the true p value within the distribution of permuted p values. We also report the combined p value of the plates, calculated using an R script developed in-house.

Slice Electrophysiology

P20–29 male and female mice were deeply anesthetized with isoflurane and decapitated. The brain was removed and 350 μm coronal slices of frontal cerebral cortex were cut in ice-cold cutting solution (126 mM NaCl, 25 mM $NaHCO_3$, 10 mM d-glucose, 3.5 mM KCl, 1.5 mM NaH_2PO_4, 0.5 mM $CaCl_2$, 10.0 mM $MgCl_2$) with a Leica VT1000S. Slices were then transferred to a storage chamber with fresh artificial cerebrospinal fluid (aCSF) containing 126 mM NaCl, 3.5 mM KCl, 1.0 mM $MgCl_2$, 2.0 mM $CaCl_2$, 1.5 mM NaH_2PO_4, 25 mM $NaHCO_3$, and 10 mM d-glucose, pH 7.3-7.4, and were incubated at 37°C for 30 min. The slices were then incubated at room temperature for at least another 30 min before recording. All solutions were continuously bubbled with 95% O_2 and 5% CO_2.

Whole-cell current-clamp and recordings were obtained from cortical layer 2/3 pyramidal cells and interneurons at 32°C using a Multiclamp 700B and Clampex 10.5 software (Molecular Devices). Individual slices were transferred to a recording chamber located on an upright microscope (BX51; Olympus) and were perfused with oxygenated aCSF (2 mL/min). Neurons were visualized using IR-

differential interference contrast microscopy. Layer 2/3 pyramidal cells were distinguished from interneurons by their triangular morphology, large soma, and pronounced apical dendrite. NFS GABAergic cells were distinguished from pyramidal neurons by their typical ovoid-shaped cell bodies and were finally confirmed by electrophysiological recordings as displaying shorter AP half-widths and higher peak AP frequency (Avermann et al., 2012). Intracellular solution contained (in mM): 136 mM K-gluconate, 17.8 mM HEPES, 1 mM EGTA, 0.6 mM MgCl2, 4 mM ATP, 0.3 mM GTP, 12 mM creatine phosphate, and 50 U/ml phosphocreatine kinase, pH 7.2. When patch electrodes were filled with intracellular solution, their resistance ranged from 4–6 MΩ. Access resistance was monitored continuously for each cell. The protocols and determination of electrophysiological parameters were conducted as described above for the culture recordings. All experiments were performed and analyzed by an investigator blinded to the animal genotypes.

QUANTIFICATION AND STATISTICAL ANALYSIS

Prism 7 (GraphPad Prism, RRID:SCR_002798) was used to perform statistical tests on adult behavioral tests and to create all graphs. Multiple group comparisons were done using two-tailed t test with correction using the Holm-Sidak method, Mann-Whitney U test, or two-way repeated-measures ANOVA with correction using the Sidak's test, as indicated. Statistics for MEA data and seizure frequency were performed in R using a Mann-Whitney U test with 1,000 permutations.

To test for statistical significance for all whole cell electrophysiology experiments, we used generalized linear mixed models (GLMM) in SPSS (26.0 Chicago, Ill (IBM, RRID:SCR_002865), which allows for within-subject correlations and the specification of the most appropriate distribution for the data. Because neurons and animals from the same culture or animal are not independent measurements, culture or litter was used as the subject variable, and animals and neurons were considered within-subject measurements. All data distributions were assessed with the Shapiro-Wilk test. Datasets that were significantly different from the normal distribution ($p < 0.05$) were fit with models using the gamma distribution and a log link function, except for synaptic connection probability, which was fit with the binomial distribution and probit link. Normal datasets were fit with models using a linear distribution and identity link. We used the model-based estimator for the covariance matrix and goodness of fit was determined using the corrected quasi likelihood under independence model criterion and by the visual assessment of residuals. All values reported in the text, figures, and tables are estimated marginal means ± standard error.